

**Eckhaus instability and homoclinic snaking**

A. Bergeon

*IMFT UMR CNRS 5502–UPS UFR MIG, 31062 Toulouse Cedex, France*

J. Burke

*Boston University, Center for BioDynamics, 111 Cummington Street, Boston, Massachusetts 02215, USA*

E. Knobloch

*Department of Physics, University of California, Berkeley, California 94720, USA*

I. Mercader

*Departament de Física Aplicada, Universitat Politècnica de Catalunya, Barcelona, Spain*

(Received 23 June 2008; published 1 October 2008)

Homoclinic snaking is a term used to describe the back and forth oscillation of a branch of time-independent spatially localized states in a bistable, spatially reversible system as the localized structure grows in length by repeatedly adding rolls on either side. This behavior is simplest to understand within the subcritical Swift-Hohenberg equation, but is also present in the subcritical regime of doubly diffusive convection driven by horizontal gradients. In systems that are unbounded in one spatial direction homoclinic snaking continues indefinitely as the localized structure grows to resemble a spatially periodic state of infinite extent. In finite domains or in periodic domains with finite spatial period the process must terminate. In this paper we show that the snaking branches in general turn over once the length of the localized state becomes comparable to the domain, and examine the factors that determine the location of the termination point or points, and their relation to the Eckhaus instability of the spatially periodic state.

DOI: [10.1103/PhysRevE.78.046201](https://doi.org/10.1103/PhysRevE.78.046201)

PACS number(s): 47.54.-r, 47.20.Ky, 44.25.+f

**I. INTRODUCTION**

Stationary spatially localized states are of great interest in the theory of pattern formation. Such states occur not only in vibrating granular media [1] and polymeric fluids [2], but also in reaction-diffusion systems [3], nonlinear optics [4], ferrofluids [5], and in several convection systems, both in two and three dimensions [6–10]. In one dimension these systems have two properties in common: they are reversible in space (i.e., invariant under the reflection  $x \rightarrow -x$ , together with the corresponding change in the dependent variables), and bistable (i.e., there is a parameter regime in which a trivial spatially homogeneous state coexists with a spatially periodic steady state).

In the standard picture of unbounded systems of this type spatially localized states first appear via a bifurcation from the trivial state and do so simultaneously with the primary branch of spatially periodic states. Typically there are two branches of spatially localized states that are produced, with either global maxima or global minima at the midpoint  $x = 0$ . These states are distinct, and are not related by symmetry. The branches of localized states bifurcate in the same direction as the periodic states, i.e., subcritically, and are initially unstable. With decreasing parameter the localized states grow in amplitude but shrink in extent; when the extent of the localized state approaches one wavelength and the amplitude reaches that of the competing periodic state the branch enters the so-called snaking or pinning region, and begins to “snake” back and forth. As this happens the localized state gradually adds rolls, symmetrically on either side, thereby increasing its length. As a result the localized states high up the snaking branches resemble the finite amplitude

spatially periodic state over longer and longer lengths. Typically each snaking branch repeatedly gains and loses stability via saddle node bifurcations, producing an infinite multiplicity of coexisting stable states within the pinning region. Secondary bifurcations to pairs of (unstable) branches of asymmetric states are found in the vicinity of each saddle node; these branches resemble “rungs” that connect the two snaking branches and are responsible for the “snakes-and-ladders” structure of the localized states [11,12]. The origin and properties of this behavior are now quite well understood, at least in variational systems [13–15].

In this paper we find it useful to adopt a complementary view, based on the observation that a second bifurcation to spatially localized states is present as well. This bifurcation typically occurs near the saddle node bifurcation on the primary branch of periodic states, and the resulting spatially localized states resemble extended “holes” in a background of otherwise spatially periodic finite amplitude wave trains [16]. These branches also appear as a pair, and also enter the snaking region where they snake, as the hole deepens and becomes filled with longer and longer sections of the trivial state. At present, our understanding of the behavior of the holelike states is incomplete although the work described in this paper identifies several key elements critical to a proper description of these states.

On an unbounded domain these two pairs of snaking branches remain distinct. This is not so, however, once the domain becomes finite. In this case neither set of branches can snake forever, and the snaking process must terminate when the width of the localized periodic state approaches the domain size, and likewise for the width of the localized hole. Thus both pairs of branches must turn over and exit the snak-

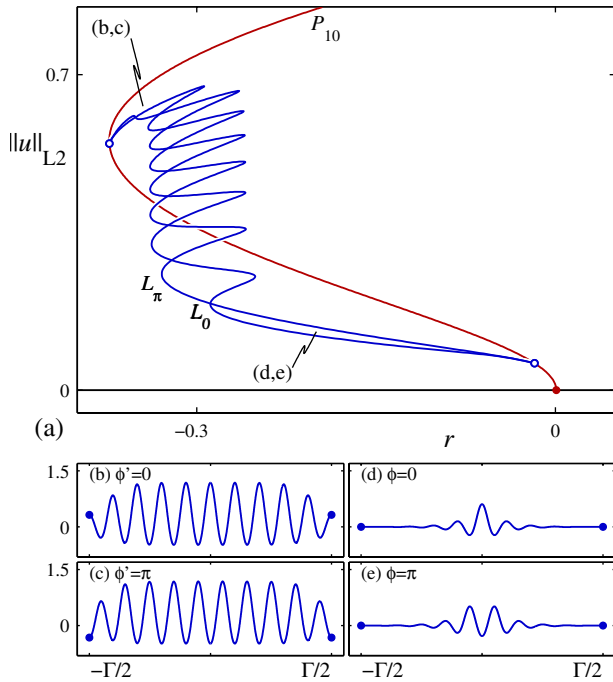


FIG. 1. (Color online) (a) Bifurcation diagram showing the equivalent of homoclinic snaking on a periodic domain with period  $\Gamma$ . The snaking branches  $L_0$  and  $L_\pi$  emerge from  $P_{10}$ , a branch of periodic states with ten wavelengths within  $\Gamma$ , in a secondary bifurcation ( $\circ$ ) at small amplitude, and terminate on the same branch in a secondary bifurcation ( $\circ$ ) near the saddle node. Other spatially periodic branches are also present, but for clarity are not shown. (b), (c) Sample profiles from the  $\phi'=0$  and  $\phi'=\pi$  branches near the upper end of the snaking branches. (d), (e) Sample profiles from the  $\phi=0$  and  $\phi=\pi$  branches on the lower part of the snaking branches. In this case the  $L_0$  branch connects the  $\phi=0$  and  $\phi'=0$  solutions, and the  $L_\pi$  branch connects the  $\phi=\pi$  and  $\phi'=\pi$  solutions. In this and other figures, the boundaries of the profiles are indicated by  $\bullet$ . The figure is computed using Eq. (1) with  $f(u)=b_2u^2-u^3$ ,  $b_2=1.8$ , on a periodic domain with  $\Gamma=62$ .

ing region. Typically the two pairs of branches connect pairwise, so that the small amplitude branch with maxima at  $x=0$  now connects to the corresponding branch of holelike states, and likewise for the branch with minima at  $x=0$  (Fig. 1). This figure, computed for the quadratic-cubic Swift-Hohenberg equation on a periodic domain of period  $\Gamma$ , shows that the classic localized states enter the pinning region from small amplitude on the right and exit this region at large amplitude toward the left; however, the same figure can also be viewed as showing that the holelike states enter the snaking region at the top from the left and exit it near the bottom toward the right. One finds, in addition, that in domains of finite size, the branches of small amplitude localized states no longer bifurcate directly from the trivial state, but now do so in a secondary bifurcation on the primary branch of periodic states. The finite domain size likewise affects the bifurcation to the holelike states on the branch of periodic states. However, overall in domains of finite but large size the behavior within the snaking region remains essentially identical to that present on the real line, with the effects of the finite size confined to the vicinity of the bifur-

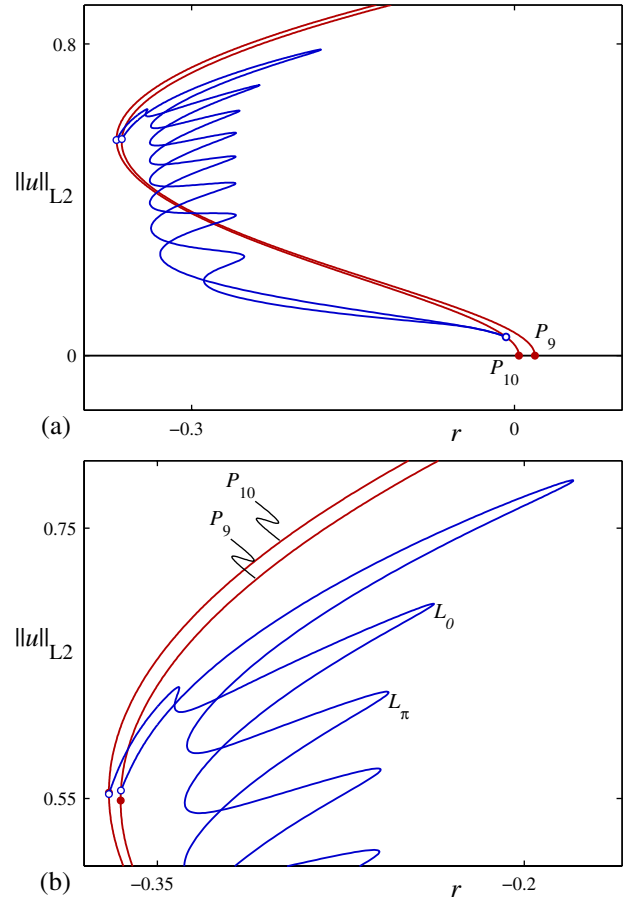


FIG. 2. (Color online) (a) Bifurcation diagram at a value of  $\Gamma$  where the two snaking branches terminate on different spatially periodic branches. Both snaking branches emerge from  $P_{10}$ . (b) Detail showing that the  $L_0$  snaking branch terminates below the saddle node on  $P_{10}$ , while the  $L_\pi$  snaking branch terminates above the saddle node on  $P_9$ . Other, mixed mode branches (not shown) also emerge from each of the large amplitude secondary bifurcations but do not snake. Parameters:  $b_2=1.8$ ,  $\Gamma=60.9$ .

cations creating the localized and holelike states in the first place. In particular the snaking structure of the pinning region persists in finite size domains, although the structure is necessarily truncated. We do not consider here finite size effects on the rung states since these are unstable.

We show here that the above picture, while largely correct, fails to describe all aspects of finite domain size. In particular, we show that in some regimes the branches terminate together, while in others they terminate on different branches of periodic states (Fig. 2), and describe the reason for this unexpected behavior. In addition, we investigate in detail the location of the termination point (or points) relative to the saddle node bifurcation(s) on the branch(es) of periodic states, and their relation to the well-known Eckhaus (or modulational) instability of periodic wave trains.

Elucidation of these issues is critical to understanding the appearance and properties of spatially localized states in more realistic systems, where the available domain may be of finite extent, or in numerical simulations where periodic domains are often used to model systems that are in fact unbounded.

This paper is organized as follows. In the next section we analyze the properties of a bistable Swift-Hohenberg equation and deduce a number of conclusions for bounded systems concerning the creation of the snaking branches at small amplitude, and their termination at large amplitude, focusing on the so-called single pulse localized states. In Sec. III we explain the relation of these results to the Eckhaus instability of the spatially periodic states, and in Sec. IV we investigate a convection system that exhibits homoclinic snaking in order to confirm that the behavior identified in the earlier sections occurs in more general pattern-forming systems. We conclude in Sec. V with a summary and discussion of the important results.

**II. SWIFT-HOHENBERG EQUATION**

The Swift-Hohenberg equation describes the formation of spatially periodic patterns with a finite wave number  $k_0$  at onset. In one spatial dimension the equation takes the form

$$u_t = ru - (\partial_x^2 + k_0^2)u + f(u). \tag{1}$$

This equation is variational and hence on finite domains all solutions approach steady states. In the following we shall be interested in characterizing such states. The key to the properties of these states is provided by the invariance of Eq. (1) under  $x \rightarrow -x, u \rightarrow u$ , hereafter referred to as “reversibility.” On the real line this property is responsible for the presence of a reversible Hopf bifurcation with 1:1 resonance in the linear stability problem of the trivial solution  $u=0$  in space. Specifically, at  $r=0$  the (four) spatial eigenvalues are given by  $\lambda = \pm ik_0$ , each with double multiplicity. Moreover, for  $r < 0$  these eigenvalues move off the imaginary axis and form a complex quartet  $[\lambda = \pm ik_0 \pm (\sqrt{-r/2k_0} + O(r))]$  while for  $r > 0$  they also split but remain on the imaginary axis  $[\lambda = \pm ik_0 \pm i(\sqrt{r/2k_0} + O(r))]$ . The presence of this bifurcation can in turn be used to show that spatially periodic and spatially localized states bifurcate simultaneously from  $u=0$  as the bifurcation parameter  $r$  is increased through  $r=0$  only in the so-called “subcritical” regime [11,14]. The latter undergo the homoclinic snaking that is of interest in the present paper.

In this paper we consider the case  $f(u) \equiv b_2 u^2 - u^3$ , which is the simplest nonlinearity that produces the bistability crucial for homoclinic snaking. In the following we scale Eq. (1) such that  $k_0=1$ , so that the equation is fully parameterized by  $r$  and  $b_2$ . Periodic solutions with this wave number set in at  $r=0$  and are followed at

$$r = (k^2 - k_0^2)^2 > 0 \tag{2}$$

by solutions with wave numbers  $k \neq k_0$ . The bifurcation at  $r=0$  is subcritical when [11,14]

$$q_2 \equiv \frac{3}{4k_0^2} - \frac{19b_2^2}{18k_0^6} < 0 \tag{3}$$

(this is the case for  $k_0=1, b_2=1.8$  used below), and the resulting  $k_0$  branch undergoes a saddle node bifurcation at  $|r| = O(k_0^4)$  and hence at  $O(k_0^2)$  amplitude whenever  $q_2 = O(k_0^{-2})$ . The  $k \neq k_0$  branches are likewise typically subcritical and undergo saddle node bifurcations.

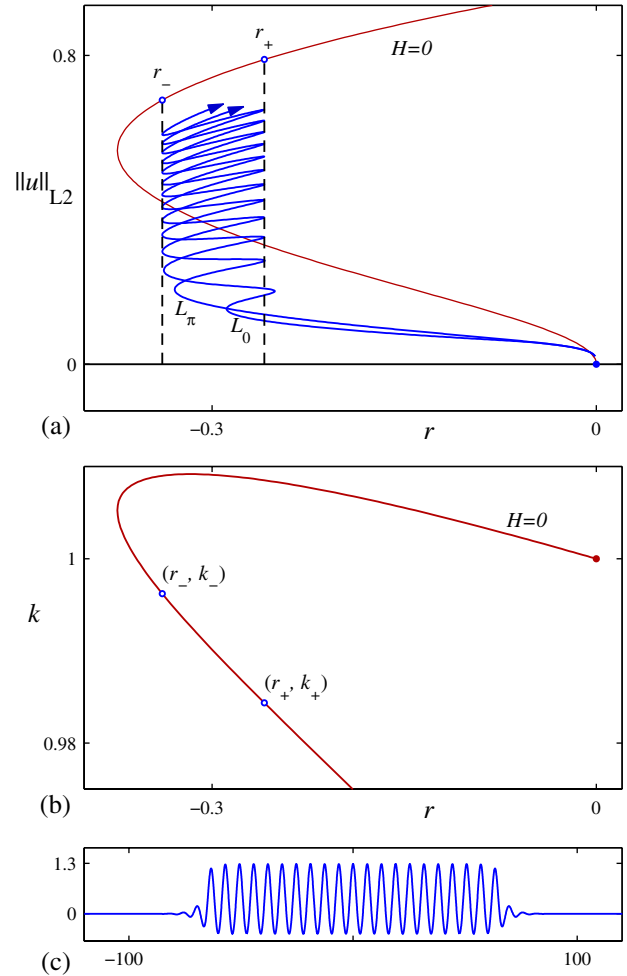


FIG. 3. (Color online) (a) Bifurcation diagram showing homoclinic snaking on an unbounded domain, including the  $L_0$  and  $L_\pi$  branches of localized states and the  $H=0$  branch of spatially periodic states. The  $L^2$ -norm of the localized states has been rescaled in order to display both classes of solutions in a single diagram. The snaking takes place in the pinning region between  $r_- = -0.3390$  and  $r_+ = -0.2593$ . (b) The wave number  $k(r)$  along the  $H=0$  spatially periodic branch. The wave number of the pattern within the localized states varies between  $k_+ \approx 0.9843 \equiv k_L$  and  $k_- \approx 0.9962$ . (c) A broad localized state at  $r = -0.312$ , from the  $L_0$  snaking branch. Parameter:  $b_2 = 1.8$ .

On the real line, the localized states of interest approach  $u=0$  as  $x \rightarrow \pm \infty$ . In  $q_2 < 0$ , a pair of such branches emerges subcritically from the trivial state in a pitchfork bifurcation at  $r=0$ . Near onset ( $|r| \ll 1$ ) these are given by

$$u(x) = \frac{1}{k_0} \left( \frac{2r}{q_2} \right)^{1/2} \operatorname{sech} \left( \frac{x\sqrt{-r}}{2k_0} \right) \cos(k_0 x + \phi) + O(r), \quad r < 0, \tag{4}$$

where  $\phi=0, \pi$  are the only values of the spatial phase  $\phi$  for which expression (4) approximates true solutions of Eq. (1) [11]. We define  $L_0$  and  $L_\pi$  as the branches of reflection symmetric localized states found by continuing Eq. (4) with  $\phi = 0, \pi$  to finite amplitude (Fig. 3). Along  $L_0$  the midpoint  $x = 0$  of the localized state is always a global maximum, while

along  $L_\pi$  it is a global minimum. The broad localized states found higher and higher up the two snaking branches are confined to a pinning region in  $r$ ,  $r_- < r < r_+$ . The wave number  $k(r)$  of the pattern within these states varies across this region,  $k_- > k > k_+$ . This wave number range is therefore characteristic of the localized states in the pinning region, and plays an important role in their behavior on a finite domain.

In the present case the spatial dynamical system defined by the time-independent version of Eq. (1) conserves the Hamiltonian

$$H = -\frac{1}{2}(r - k_0^4)u^2 + k_0^2 u_x^2 - \frac{1}{2}u_{xx}^2 + u_x u_{xxx} - \int_0^u f(v)dv. \quad (5)$$

Since  $H$  vanishes on the trivial state  $u=0$  it follows that any broad localized state consisting of heteroclinic connections from  $u=0$  to a periodic orbit and back again must lie in the surface  $H=0$ . The spatially periodic branch selected by this criterion is shown in Fig. 3(a) and the corresponding wave number  $k(r)$  is shown in Fig. 3(b). The predicted wave number agrees very well with the wave number measured in broad localized states such as the one shown in Fig. 3(c). Thus the presence of the fronts at either end of the localized state selects a unique wave number. Wave number selection in systems without a conserved Hamiltonian is not understood.

Throughout the remainder of the paper we make use of two scalar measures of solutions to Eq. (1), the  $L^2$ -norm and the sup-norm, defined by

$$\|u\|_{L^2} \equiv \left( \frac{1}{\Gamma} \int_0^\Gamma u^2(x)dx \right)^{1/2}, \quad \|u\|_{\text{sup}} \equiv \max[u(x)]. \quad (6)$$

The former distinguishes between different states on the snaking branches, while the latter provides a better measure of the solution amplitude.

### A. Small amplitude localized states

On a finite domain of size  $\Gamma \gg 2\pi/k_0$  only a discrete number of spatially periodic branches is present. We introduce the notation  $P_n$  to describe the spatially periodic branch with fixed wave number  $k=2\pi n/\Gamma$ , where  $n$  is an integer. The  $P_n$  branch therefore contains  $n$  wavelengths in the domain  $\Gamma$ . The locus of the primary bifurcations to these allowed branches is determined by Eq. (2), and is shown in Fig. 4(a) as a function of  $\Gamma$ . For each  $n$  the resulting curve is tangent to  $r=0$  at  $\Gamma=2\pi n/k_0$ . Long wave modulational instabilities lead to secondary bifurcations along the spatially periodic branches which play a crucial role in what follows. In general, we refer to a secondary bifurcation involving modulation over  $n$  wavelengths of a finite amplitude pattern as  $S^{(n)}$ ; when present on the  $P_n$  branch this bifurcation leads to states with minimal spatial period  $\Gamma$ .

On a finite domain, expression (4) is no longer valid but we can still use the  $L_0$  ( $L_\pi$ ) notation to refer to branches of symmetric localized states centered on a local maximum (minimum). In this case the snaking branches emerge instead

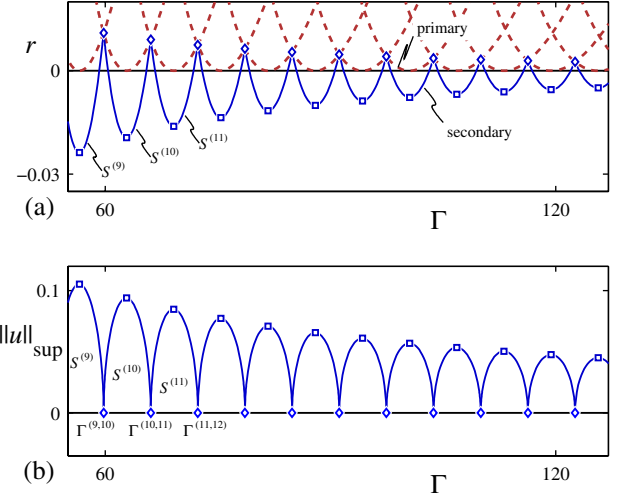


FIG. 4. (Color online) Location of the small amplitude secondary bifurcations  $S^{(n)}$  as a function of  $\Gamma$ , shown in terms of (a) the bifurcation parameter  $r$  and (b) the amplitude  $\|u\|_{\text{sup}}$  (solid lines). The critical values  $\Gamma^{(n,n+1)}$  (marked by  $\diamond$ ) divide  $\Gamma$  into regions of fixed  $n$ . Secondary bifurcations on the  $k_0$  primary branch (i.e., for  $\Gamma=2\pi n/k_0$ ) are indicated by the symbol  $\square$ . For reference, the primary bifurcations from the trivial state are also indicated [(a), dashed lines]. Parameter:  $b_2=1.8$ .

from one of the spatially periodic branches  $P_n$  in a secondary bifurcation  $S^{(n)}$  that occurs at small amplitude. The selection rules that determine  $n$  at each value of  $\Gamma$  are described below. The location in  $r$  of the secondary bifurcation point is plotted in Fig. 4 as a function of  $\Gamma$ , along with the sup-norm of the solution at this point. There is, however, an important sequence of values of  $\Gamma$  for which the branches of localized states emerge directly from the trivial state. These correspond to codimension-two points at which the trivial state loses stability simultaneously to  $P_n$  and  $P_{n+1}$ . The codimension-two points are indicated in Fig. 4 by the symbol  $\diamond$  and occur at

$$\Gamma^{(n,n+1)} = \frac{2\pi}{k_0} \left( n^2 + n + \frac{1}{2} \right)^{1/2}, \quad r^{(n,n+1)} = k_0^4 \left( \frac{n + 1/2}{n^2 + n + 1/2} \right)^2. \quad (7)$$

As shown in Fig. 5 at  $\Gamma^{(9,10)}$ , the two branches of localized states that emerge from this multiple bifurcation point resemble, near onset, one “beat” of the superposition of the two patterns, but their shape is truncated by the finite domain size. Nonetheless, on  $L_0$  the beat is centered on a global maximum, while on  $L_\pi$  it is centered on a global minimum. Further away from the primary bifurcation, in  $k_0^2 \Gamma^{-2} \ll r \ll k_0^4$ , the solutions begin to resemble those familiar from unbounded domains, described by Eq. (4). Once  $|r|=O(k_0^4)$  the states are localized within an  $O(k_0^{-1})$  interval with  $O(k_0^0)$  peak amplitudes, and both branches enter the pinning region and undergo snaking.

At intermediate values of  $\Gamma$ , where the branches of localized states bifurcate at finite amplitude from one of the spatially periodic branches, we find that only one secondary bifurcation  $S^{(n)}$  is present whose minimal period matches the

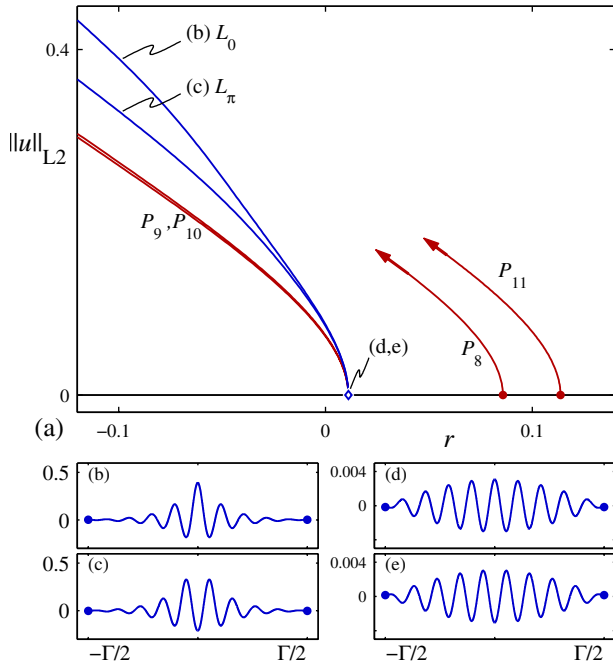


FIG. 5. (Color online) (a) Bifurcation diagram for the small amplitude states at  $\Gamma=\Gamma^{(9,10)}$ . The spatially periodic branches  $P_9$  and  $P_{10}$  emerge from the trivial state along with the localized branches  $L_0$  and  $L_\pi$  at  $r^{(9,10)}$ , indicated by  $\diamond$ . Other spatially periodic branches allowed at this  $\Gamma$  are also indicated. Profiles from the localized branches are shown (b), (c) far from onset and (d), (e) near onset. Parameters:  $b_2=1.8$ ,  $\Gamma=59.773$ .

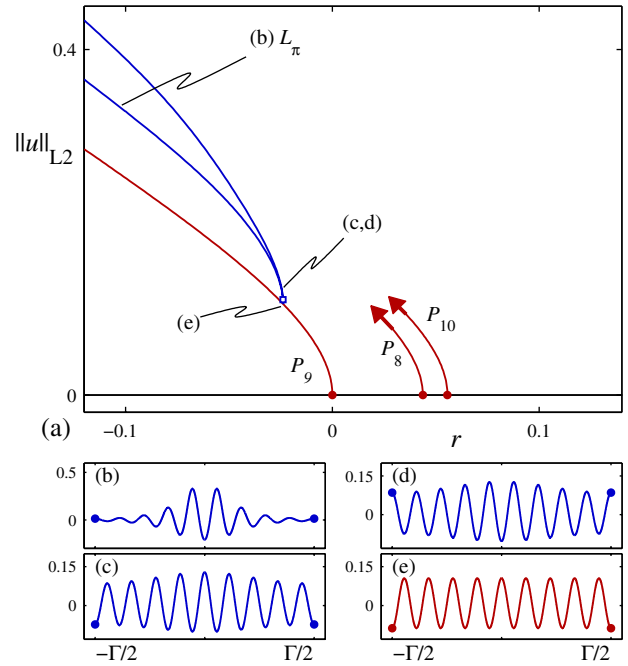


FIG. 6. (Color online) (a) Bifurcation diagram of small amplitude states at  $\Gamma=2\pi n/k_0$ , where  $n=9$ . The branches of localized states emerge from  $P_9$  at  $S^{(9)}$  ( $\square$ ). (b) Profile on the  $L_\pi$  localized branch far from onset. (c), (d) Profiles on the branches of localized states near onset. (e) Profile on  $P_9$  at the secondary bifurcation point. Parameters:  $b_2=1.8$ ,  $\Gamma=56.54$ .

domain size  $\Gamma$ , and that it always occurs on the *first* of the spatially periodic branches encountered as  $r$  increases. Thus the selection rule that determines  $n$  at each  $\Gamma$  is given by the condition that  $\Gamma^{(n-1,n)} < \Gamma < \Gamma^{(n,n+1)}$ . For example, the domain used in Fig. 6 is  $\Gamma=56.54$ , which lies between  $\Gamma^{(8,9)}=53.3$  and  $\Gamma^{(9,10)}=59.8$ , so in this case the localized branches emerge from  $P_9$  at  $S^{(9)}$ .

In Fig. 4, the locus of secondary bifurcations for fixed  $n$  forms a curve connecting  $\Gamma^{(n-1,n)}$  and  $\Gamma^{(n,n+1)}$ . Within each region of fixed  $n$  there is a value of  $\Gamma=2\pi n/k_0$  for which  $S^{(n)}$  lies on the  $k_0$  spatially periodic branch (indicated by  $\square$ ). As  $\Gamma \rightarrow \infty$  these locations approach the minima of the curves in Fig. 4(a) and maxima of the curves in Fig. 4(b). This particular sequence of secondary bifurcations obeys a power-law scaling

$$r \propto -\Gamma^\eta, \tag{8}$$

where  $\eta \approx -2$  [Fig. 7(a)]. When  $S^{(n)}$  lies instead on a branch with  $k \neq k_0$  (this occurs when  $\Gamma=2\pi n/k$ ) the scaling law no longer applies. However, regardless of the aspect ratio  $\Gamma$ , far from onset the modulated states become highly localized and undergo snaking, as in Fig. 1.

The wave number  $k$  of the  $P_n$  branch varies with  $\Gamma$  at fixed  $n$ , so an alternative way of plotting the information from Fig. 4(b) is shown in Fig. 8. Each vertical slice through this plot indicates the secondary bifurcations  $S^{(n)}$  on the corresponding  $k$  spatially periodic branch as  $\Gamma$  increases in increments of  $2\pi/k$ . The figure shows that the  $k_0$  branch is the

only one that contains secondary bifurcations associated with arbitrarily large  $n$  (indicated by  $\square$ ); any  $k$  branch with  $k \neq k_0$  involves only a finite number of secondary bifurcations up to a maximum  $n$ , determined by Eq. (7). For example,  $S^{(10)}$  is present on the  $P_{10}$  branch for  $\Gamma^{(9,10)} < \Gamma < \Gamma^{(10,11)}$ , and therefore only occurs on branches whose wave number is in the range  $0.9513 < k < 1.0512$ . The  $S^{(10)}$  secondary bifurcation is absent on all branches whose wave number lies outside this range, including the  $P_{10}$  branch in Fig. 6 for which  $k \cong 1.11$ .

Some of this behavior can be understood using perturbation theory. We define the small parameter  $\epsilon \equiv (2\pi/k_0)/\Gamma$ ,

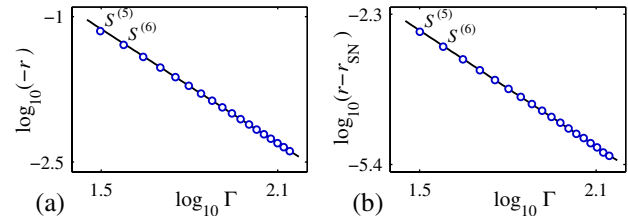


FIG. 7. (Color online) (a) Location  $r$  of the secondary bifurcations  $S^{(n)}$  that occur at small amplitude along the spatially periodic branch with wave number  $k_0$  as a function of  $\Gamma$ , shown on a log-log plot. The best fit for the exponent in Eq. (8) is  $\eta \approx -1.963$ . (b) Location  $r$  of the secondary bifurcations  $S^{(n)}$  that occur at large amplitude along the spatially periodic branch with wave number  $k_P$  relative to the value at the saddle node  $r_{SN}$ , shown as a function of  $\Gamma$  on a log-log plot. The best fit for the exponent in Eq. (18) is  $\eta \approx -3.9966$ . Parameter:  $b_2=1.8$ .

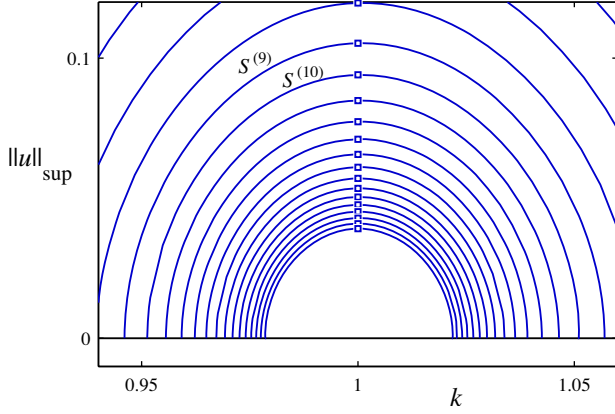


FIG. 8. (Color online) As in Fig. 4(b) but plotted in terms of the wave number  $k$  of the spatially periodic branch. The secondary bifurcations  $S^{(n)}$  for  $n > 23$  are not shown but occupy the void near the origin.

write  $r \equiv \epsilon^2 \mu$ , and look for stationary solutions to Eq. (1) of the form

$$u(x, X) = \epsilon [A(X)e^{ik_0 x} + \text{c.c.}] + O(\epsilon^2), \quad (9)$$

where  $X = \epsilon x$  is the long length scale over which the amplitude of the pattern changes, as set by the size of the domain  $\Gamma$ . It follows that [11]

$$A_{XX} = -\frac{\mu}{4k_0^2} A + q_2 |A|^2 A. \quad (10)$$

The spatial periodicity  $\Gamma$  of  $u(x)$  translates into the requirement

$$A(X + \epsilon\Gamma) = A(X)e^{-ik_0\Gamma}, \quad (11)$$

valid for all  $X$ . In the following we focus on two cases characterized by constant phase  $\arg A$ . In each case we restrict attention to even solutions, i.e., solutions invariant under  $X \rightarrow -X$ . In the first case  $\Gamma = 2\pi(n+1/2)/k_0$  (so that  $\epsilon^{-1} = n + 1/2$ ) and hence  $\exp -ik_0\Gamma = -1$ . The amplitude  $A$  thus satisfies the boundary conditions

$$A(\epsilon\Gamma/2) = -A(-\epsilon\Gamma/2), \quad A_X(\epsilon\Gamma/2) = -A_X(-\epsilon\Gamma/2). \quad (12)$$

In this case Eqs. (10) and (12) have the even solution

$$A(X) = a_1 \text{cn}(\kappa_1 X | m), \quad (13)$$

where the boundary conditions are satisfied by choosing the domain to accommodate only half a period of the  $\text{cn}(\dots)$  envelope. The coefficients in Eq. (13) are determined by

$$1 - 2m = \frac{\mu}{4k_0^2 \kappa_1^2}, \quad 2m = -\frac{q_2 a_1^2}{\kappa_1^2}, \quad 2K(m) = \epsilon \kappa_1 \Gamma, \quad (14)$$

where  $K(m)$  is the complete elliptic integral of the first kind and  $0 \leq m \leq 1$ . As  $m \rightarrow 0$ ,  $\kappa_1 \rightarrow k_0/2$  so that  $a_1 \rightarrow 0$  and  $\mu \rightarrow k_0^4$ , corresponding to a bifurcation from  $u=0$  at  $r = k_0^4(n+1/2)^{-2}$ . This is nothing but the large  $n$  limit of Eq. (7). Near the bifurcation point ( $m \ll 1$ ) the envelope in Eq. (13) re-

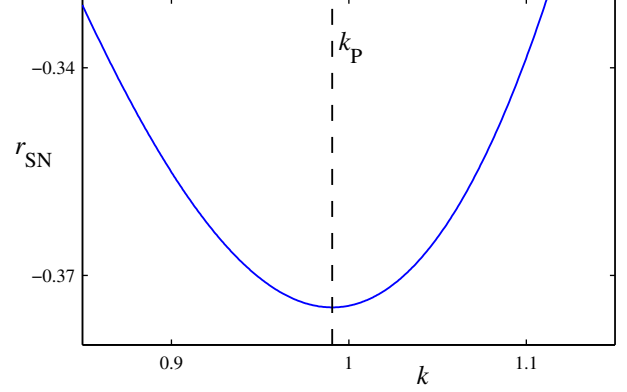


FIG. 9. (Color online) Location  $r_{\text{SN}}$  of the saddle node of spatially periodic states as a function of the wave number  $k$ . The dashed vertical line marks the minimum of  $r_{\text{SN}}$ , which defines the critical wave number  $k_p \approx 0.9906$ . Parameter:  $b_2 = 1.8$ .

duces to  $u(x) \sim \cos(\pi x/\Gamma)$ , consistent with the profiles near onset shown in Figs. 5(d) and 5(e).

If instead we choose the domain  $\Gamma$  such that  $\Gamma = 2\pi n/k_0$  then  $\epsilon^{-1} = n$  and  $\exp -ik_0\Gamma = +1$ . In this case

$$A(\epsilon\Gamma/2) = A(-\epsilon\Gamma/2), \quad A_X(\epsilon\Gamma/2) = A_X(-\epsilon\Gamma/2), \quad (15)$$

and Eqs. (10) and (15) have the solution

$$A(X) = a_2 \text{dn}(\kappa_2 X | m), \quad (16)$$

where the boundary conditions are satisfied by choosing the domain to accommodate one period of the  $\text{dn}(\dots)$  envelope. The coefficients in Eq. (16) are determined by

$$2 - m = -\frac{\mu}{4k_0^2 \kappa_2^2}, \quad 2 = -\frac{q_2 a_2^2}{\kappa_2^2}, \quad 2K(m) = \epsilon \kappa_2 \Gamma. \quad (17)$$

As  $m \rightarrow 0$ ,  $\kappa_2 \rightarrow k_0/2$  so that  $\mu \rightarrow -2k_0^4$ . In this limit the solution (16) approaches the branch of  $X$ -independent solutions to Eq. (10),  $A(X) = a_2 = k_0/\sqrt{-2q_2}$ . It follows that, in the limit of large  $n$ , the secondary bifurcations  $S^{(n)}$  which occur along the spatially periodic branch with wave number  $k_0$  do so at  $r = -2k_0^4/n^2$ . Rewriting this result in terms of the domain size yields  $r \propto \Gamma^{-2}$ , a result that is consistent with the scaling measured in Eq. (8). Near onset ( $m \ll 1$ ), Eq. (16) also reproduces the weak modulation of the envelope shown in Fig. 6. Far from onset both Eqs. (13) and (16) approach the  $\text{sech}(\dots)$  form valid when the width of the localized state is smaller than  $\Gamma$ .

Additional solutions in which  $\arg A$  changes by  $2\pi, 4\pi, \dots$ , over the domain  $\Gamma$  are also present. For other aspect ratios (i.e., when  $k_0\Gamma \neq 0, \pi \pmod{2\pi}$ ) the amplitude  $A(X)$  is necessarily complex, and the relevant solutions are of phase-winding type [17].

## B. Large amplitude localized states

As mentioned above, each spatially periodic branch that emerges subcritically from the trivial state undergoes a saddle node bifurcation. The location  $r_{\text{SN}}$  of the saddle node varies with wave number as shown in Fig. 9. The minimum of this function defines a new critical wave number  $k_p$

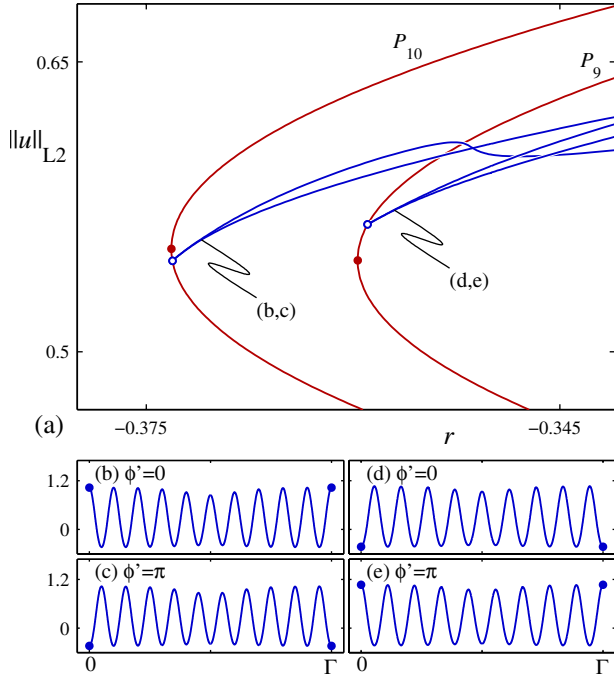


FIG. 10. (Color online) Bifurcation diagram at  $\Gamma=62$ , in the neighborhood of the large amplitude secondary bifurcations that occur near the saddle nodes (●) on the spatially periodic branches. Secondary bifurcation points are indicated by the symbol ○. Profiles are shown near onset on the secondary branches that emerge (b),(c) from  $P_{10}$  at  $S^{(10)}$  and (d),(e) from  $P_9$  at  $S^{(9)}$ . Parameters:  $b_2=1.8$ ,  $\Gamma=62$ .

$\approx 0.9906$  which plays a similar role at large amplitude to  $k_0$  at small amplitude. In the limit of small  $q_2$  these two critical wave numbers are equal but at finite  $q_2$  they differ due to nonlinear effects.

Once again we shall be interested in secondary bifurcations  $S^{(n')}$  involving modulation over an integer  $n'$  wavelengths of a spatially periodic pattern, though now we focus on the bifurcations present at  $O(1)$  amplitude. In this case we find that *each* of the spatially periodic branches  $P_{n'}$ , allowed by  $\Gamma$  contains one secondary bifurcation  $S^{(n')}$  at  $O(1)$  amplitude. Figure 10 shows a typical bifurcation diagram: the secondary bifurcation on the first spatially periodic branch encountered as  $r$  increases lies below the saddle node, while those on subsequent branches lie above. Some of these occur at very large amplitude, though we are interested primarily in the ones that occur in the neighborhood of the saddle nodes. The secondary bifurcations  $S^{(n')}$  are shown in Fig. 11 as a function of  $\Gamma$ , and in Fig. 12 as a function of  $k$ . Both figures show the sup-norm of the secondary bifurcation point relative to the value at the saddle node on the corresponding spatially periodic branch,  $\|u\|_{\text{sup}} - \|u_{\text{SN}}\|_{\text{sup}}$ .

The secondary bifurcations that occur on a spatially periodic branch with fixed  $k$  for different  $\Gamma$  (equivalently  $n'$ ) follow from Fig. 12. On the  $k_p$  branch, present when  $\Gamma = 2\pi n'/k_p$ , these always lie below the saddle node but accumulate on it as  $n'$  increases [Fig. 13(a)]. The distance between the secondary bifurcation and the saddle node appears to obey a power-law scaling

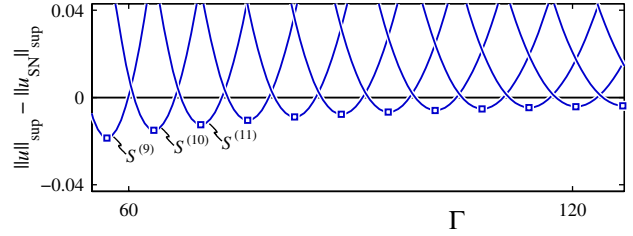


FIG. 11. (Color online) Location of  $S^{(n')}$  as a function of  $\Gamma$ , plotted in terms of the amplitude at the bifurcation point  $\|u\|_{\text{sup}}$  relative to the saddle node  $\|u_{\text{SN}}\|_{\text{sup}}$ . The secondary bifurcations that lie along the  $k_p$  spatially periodic branch are marked with a □. Parameter:  $b_2=1.8$ .

$$\|u\|_{\text{sup}} - \|u_{\text{SN}}\|_{\text{sup}} \propto -\Gamma^{\eta/2}, \quad r - r_{\text{SN}} \propto \Gamma^{\eta}, \quad (18)$$

where  $\eta \approx -4$  [Fig. 7(b)]. Here the “SN” subscripts refer to values at the saddle node of the  $k_p$  spatially periodic branch, and the scaling is given in terms of both the amplitude and the bifurcation parameter  $r$  at the secondary bifurcation point. The same sequence of secondary bifurcations is present along the other periodic branches with fixed  $k \neq k_p$  but the accumulation point  $\|u^*\|_{\text{sup}}$  moves above the saddle node [Fig. 13(b)]. In this case most of the secondary bifurcations occur above the saddle node but some occur below; for example, on the  $k \approx 1.031k_p$  branch shown in Fig. 13(b),  $S^{(n')}$  occurs below the saddle node when  $n' \leq 14$  and above for  $n' \geq 15$ . It turns out that for  $k \neq k_p$  the bifurcations continue to accumulate at  $\|u^*\|_{\text{sup}}$  at a geometric rate with the *same* exponent  $\eta$ . This is a consequence of the (empirical) fact that the bifurcation loci for different values of  $n'$  in Fig. 12 are nothing but vertical shifts of the accumulation locus. The geometric rate of accumulation in  $r$  changes to  $\eta/2$  on

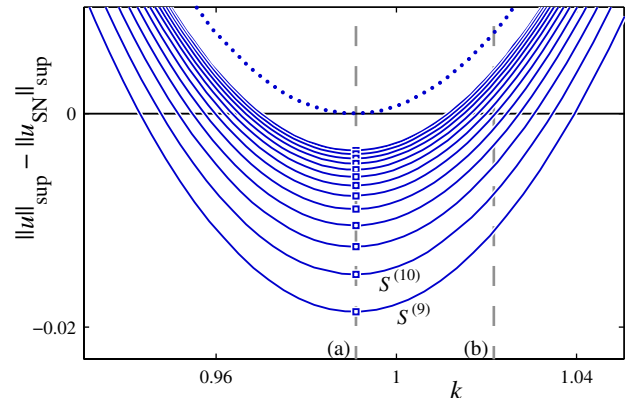


FIG. 12. (Color online) As in Fig. 11 but plotted in terms of the wave number  $k$ . The locus of accumulation points  $\|u^*\|_{\text{sup}}$  for large  $\Gamma$  is also indicated (dotted line). All curves are related by vertical shift to within numerical accuracy. The secondary bifurcations with  $n' \geq 22$  are not shown but occupy the “U-shaped” void; no secondary bifurcations occur above the curve of accumulation points. The secondary bifurcations at  $k=k_p$  are indicated by the line marked (a) and are shown in Fig. 13(a). The secondary bifurcations at  $k \approx 1.031k_p$  are indicated by the line marked (b) and are shown in Fig. 13(b).

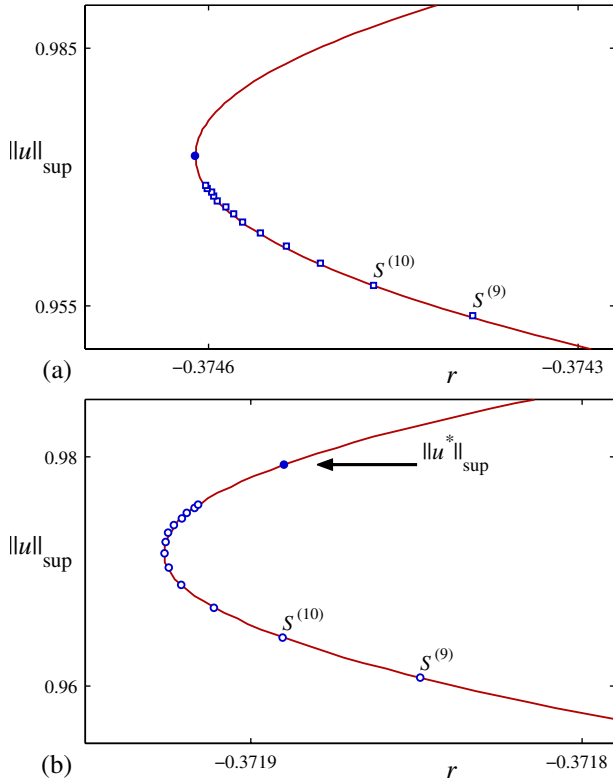


FIG. 13. (Color online) (a) Secondary bifurcations  $S^{(n')}$  along the  $k=k_p$  branch of spatially periodic states present when  $\Gamma=2\pi n'/k_p$ . These lie on the line marked (a) in Fig. 12. The accumulation point for large  $n'$  is the saddle node (●). (b) Secondary bifurcations along the  $k \approx 1.031k_p$  branch of spatially periodic states, present when  $\Gamma=2\pi n'/k$ . These lie on the line marked (b) in Fig. 12, and the accumulation point for large  $n'$  lies above the saddle node at  $\|u^*\|_{\text{sup}}$ . Parameter:  $b_2=1.8$ .

the  $k \neq k_p$  branch because the accumulation point is no longer a saddle node.

Each secondary bifurcation produces a pair of branches with minimum modulation period  $\Gamma$  which we label  $\phi'=0, \pi$  depending on whether the modulation is centered on a maximum or a minimum of the pattern, as in Fig. 10. Most of the secondary branches are mixed mode branches which continue to large  $r$ , where the profile resembles a localized defect in an otherwise uniform pattern of  $n'$  wavelengths. But for each  $\Gamma$  there are two branches which instead undergo snaking as the defect deepens until  $u(x) \sim 0$  and then begins to broaden, producing a hole near the center of the state. One of these connects to the  $L_0$  localized branch and one to  $L_\pi$ , as determined by  $\Gamma/2$  translation (Fig. 1).

In what follows we describe the selection rules that determine  $\phi'$  and  $n'$  associated with the termination of each of the two snaking branches as  $\Gamma$  varies. Given  $n'$  there is a simple selection rule based on geometry that determines the phases: the  $L_0$  snaking branch must connect to the  $\phi'=0$  branch when  $n'$  is even and to the  $\phi'=\pi$  branch when  $n'$  is odd, while the opposite holds for the  $L_\pi$  snaking branch. The selection rules that determine  $n'$  are more involved. The localized states within the pinning region first encounter the effects of a finite domain when the wave number of the pattern

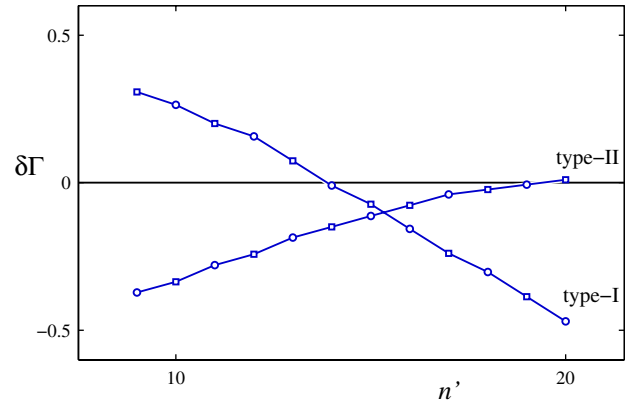


FIG. 14. (Color online) Critical values  $\Gamma_{\phi}^{(n',n'+1)}$  plotted in terms of  $\delta\Gamma \equiv \Gamma_{\phi}^{(n',n'+1)} - 2\pi(n'+1/2)/k_L$ . The symbols  $\circ$  indicate the points associated with the  $L_0$  snaking branch while the  $\square$  indicate the values associated with  $L_\pi$ . Solid lines connect points associated with transitions of the same type. Parameter:  $b_2=1.8$ .

within the state is smallest. This occurs first at  $r=r_+$  where  $k=k_+ \approx 0.9843$  [Fig. 3(b)]. Hereafter we refer to this wave number as  $k_L$ . Once this occurs the snaking branch exits the pinning region and terminates in a secondary bifurcation  $S^{(n')}$  on one of the spatially periodic branches  $P_{n'}$ , typically the one whose wave number  $k=2\pi n'/\Gamma$  is nearest to  $k_L$ . For example, when  $\Gamma=2\pi n'/k_L$  the two snaking branches both terminate on  $P_{n'}$ . Between  $\Gamma=2\pi n'/k_L$  and  $\Gamma=2\pi(n'+1)/k_L$  there is a value of  $\Gamma$  below which the  $L_0$  snaking branch terminates on  $P_{n'}$  and above which it terminates on  $P_{n'+1}$ . We define this critical value as  $\Gamma_{\phi=0}^{(n',n'+1)}$ , with a similar definition for  $\Gamma_{\phi=\pi}^{(n',n'+1)}$ . We also use the notation  $\Gamma_{\phi}^{(n',n'+1)}$  to refer to either of these two critical values when the particular phase is unimportant. These transitions occur near  $\Gamma \sim 2\pi(n'+1/2)/k_L$  but the exact location, shown in Fig. 14, must be determined numerically. Notice that  $\Gamma_{\phi=0}^{(n',n'+1)} \neq \Gamma_{\phi=\pi}^{(n',n'+1)}$  implying that the transitions on the two snaking branches do not occur simultaneously. Figure 15 combines the information from Figs. 11 and 14 to indicate graphically the selection rules that determine  $n'$  and  $\phi'$  as functions of  $\Gamma$ .

Since the value of  $k_L$  is smaller than  $k_p$ , the range in  $\Gamma$  for which the snaking branch terminates at a particular  $n'$  is consistently shifted to the right of the local minima in Fig. 15, which correspond to  $\Gamma=2\pi n'/k_p$ . At large  $n'$  the shift becomes sufficiently large to exclude the local minima from the range determined by the selection rule. Thus even though the secondary bifurcations on the  $k_p$  branch of spatially periodic states lead to snaking in the range of  $\Gamma$  considered in the figure, on yet larger domains these secondary branches will not snake and instead continue to large  $r$  as mixed mode branches. On very large domains the snaking branches terminate slightly above the saddle node of the  $k_L$  branch, as determined by the accumulation point  $\|u^*\|_{\text{sup}}$  for  $k=k_L$  in Fig. 12.

The explanation of the unusual behavior in Fig. 2 is now clear. The size of the domain in this figure lies between  $\Gamma^{(9,10)}$  and  $\Gamma^{(10,11)}$ , and the two snaking branches emerge to-

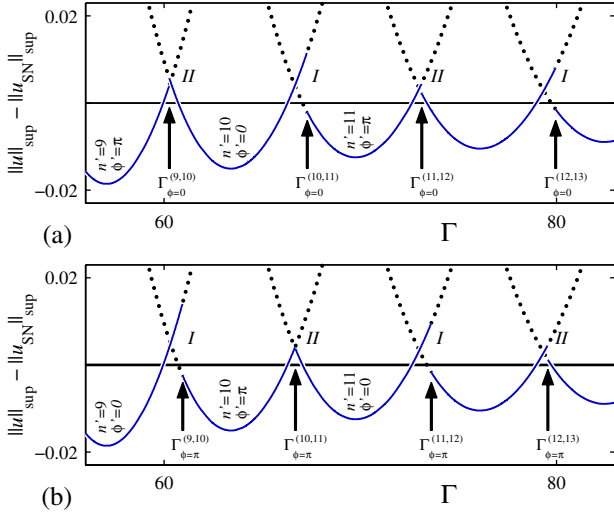


FIG. 15. (Color online) As in Fig. 11, with solid lines indicating ranges in  $\Gamma$  where the  $L_0$  and  $L_\pi$  snaking branches terminate at a particular  $S^{(n')}$ ; the phase  $\phi'$  at termination is also indicated. The discontinuities at  $\Gamma^{(n',n'+1)}$  are associated with type-I and type-II transitions (see text).

gether from  $P_{10}$  at small amplitude. This value of  $\Gamma$  is slightly above  $\Gamma_{\phi=0}^{(9,10)}$  so the  $L_0$  snaking branch terminates on  $P_{10}$ . But  $\Gamma$  also lies slightly below  $\Gamma_{\phi=\pi}^{(9,10)}$  so the  $L_\pi$  snaking branch terminates on  $P_9$ . The other, mixed mode branches (not shown) that emerge from the large amplitude secondary bifurcations continue to large  $r$  but do not snake.

The critical values  $\Gamma_{\phi}^{(n',n'+1)}$  plotted as a function of  $n'$  in Fig. 14 indicate that the transitions separate into two qualitatively different categories: type-I transitions occur at  $\Gamma_{\phi=0}^{(n',n'+1)}$  when  $n'$  is even and at  $\Gamma_{\phi=\pi}^{(n',n'+1)}$  when  $n'$  is odd, while type-II transitions occur at  $\Gamma_{\phi=0}^{(n',n'+1)}$  when  $n'$  is odd and at  $\Gamma_{\phi=\pi}^{(n',n'+1)}$  when  $n'$  is even. Each snaking branch therefore alternates between the two types of transitions as  $\Gamma$  increases. The distinction between the two types of transitions can also be described in terms of the phase  $\phi'$  of the termination point. Type-I transitions occur when a snaking branch connects to the  $\phi'=0$  branch created at  $S^{(n')}$  below the critical value  $\Gamma_{\phi}^{(n',n'+1)}$  and to the  $\phi'=\pi$  branch created at  $S^{(n'+1)}$  above  $\Gamma_{\phi}^{(n',n'+1)}$ , while the opposite case applies to type-II transitions.

The transitions at  $\Gamma_{\phi}^{(n',n'+1)}$  represent discontinuities at which the termination point of each snaking branch suddenly jumps from  $P_{n'}$  to  $P_{n'+1}$ , although each locus of secondary bifurcations in Fig. 15 varies continuously with  $\Gamma$ . This is a consequence of a reconnection process involving one of the secondary branches that emerges from  $P_{n'}$  at  $S^{(n')}$  and one from  $P_{n'+1}$  at  $S^{(n'+1)}$ . This interaction is nonlocal and resembles the unfolding of the normal form  $x^2 - \lambda^2 + \alpha = 0$  as  $\alpha$  changes sign, where  $x$  is a scalar order parameter and  $\lambda$  the bifurcation parameter [18,19]. In Eq. (1) the unfolding parameter analogous to  $\alpha$  is  $\Gamma - \Gamma_{\phi}^{(n',n'+1)}$  with the norm as the order parameter. The behavior here is further complicated by the fact that the interaction occurs in the neighborhood of a

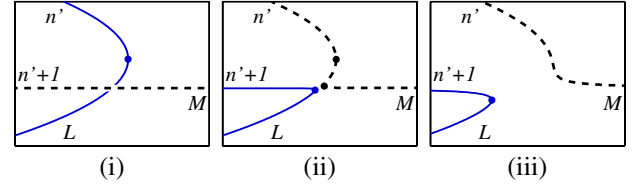


FIG. 16. (Color online) Schematic behavior of the branches in a type-I transition. The branch labels  $n'$ ,  $n'+1$ ,  $L$ , and  $M$  are defined in the text. The symbols  $\bullet$  indicate saddle node bifurcations. The bifurcation diagram in (i) corresponds to  $\Gamma < \Gamma_{\phi}^{(n',n'+1)}$ , (ii) slightly above  $\Gamma_{\phi}^{(n',n'+1)}$ , and (iii) further above  $\Gamma_{\phi}^{(n',n'+1)}$ . For clarity, the localized snaking branch is drawn as a solid line in each frame.

saddle node on one or both of the branches involved. In fact it is this property which distinguishes between the type-I and type-II transitions. An example of a type-I transition is shown schematically in Fig. 16. The subbranches involved are labeled  $n'$ ,  $n'+1$ ,  $L$ , and  $M$ , and refer, respectively, to a subbranch that terminates on  $P_{n'}$  at  $S^{(n')}$ , one that terminates on  $P_{n'+1}$  at  $S^{(n'+1)}$ , a localized snaking branch, and a mixed mode branch that extends to large  $r$ . In  $\Gamma < \Gamma_{\phi}^{(n',n'+1)}$  the  $n'$  and  $L$  subbranches connect, as do the  $n'+1$  and  $M$  branches, indicating that the localized snaking branch terminates at  $S^{(n')}$  [Fig. 16(a)]. In  $\Gamma > \Gamma_{\phi}^{(n',n'+1)}$ , the  $n'$  and  $M$  branches connect, as do the  $n'+1$  and  $L$  branches, indicating that the snaking branch terminates at  $S^{(n'+1)}$  instead [Fig. 16(b)]. This reconnection also creates a pair of saddle nodes in  $\Gamma > \Gamma_{\phi}^{(n',n'+1)}$  that were absent in  $\Gamma < \Gamma_{\phi}^{(n',n'+1)}$ . Notice also that the reconnection occurs near a saddle node of the  $n'$  subbranch, which in  $\Gamma < \Gamma_{\phi}^{(n',n'+1)}$  corresponds to the uppermost saddle node on the snaking branch. As  $\Gamma$  increases the two saddle nodes on the branch connecting  $n'$  and  $M$  annihilate in a hysteresis bifurcation [Fig. 16(c)].

An example of a type-II transition, involving the same subbranches and the same sequence of reconnection followed by hysteresis bifurcation as in the type-I transition, is shown schematically in Fig. 17. But in this case the reconnection occurs near a saddle node on each of the two branches involved, with the hysteresis bifurcation eliminating two of the saddle nodes that exist on the branch connecting  $n'+1$  and  $L$  in  $\Gamma > \Gamma_{\phi}^{(n',n'+1)}$ . Figure 18 shows the location in  $r$  of the saddle nodes during a particular type-I transition (at  $\Gamma_{\phi=0}^{(9,10)}$ ) and a particular type-II transition (at  $\Gamma_{\phi=0}^{(9,10)}$ ) as  $\Gamma$  varies. When  $n'$  is large the reconnection occurs closer to the saddle nodes for both types of transitions resulting in singular behavior as the reconnection and hysteresis bifurcations occur (almost) simultaneously.

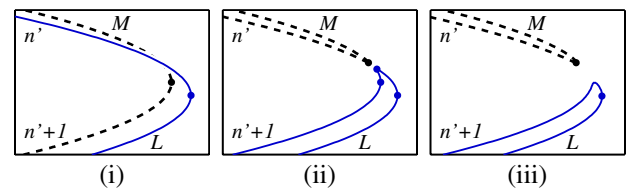


FIG. 17. (Color online) As in Fig. 16, but for a type-II transition.

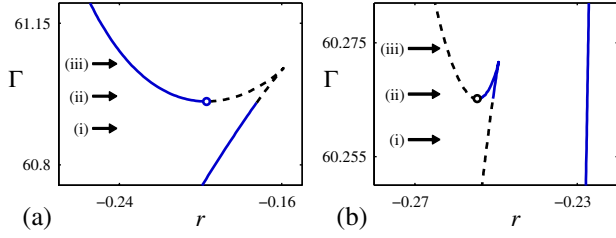


FIG. 18. (Color online) (a) Location of the saddle nodes near the type-I transition at  $\Gamma_{\phi=\pi}^{(9,10)}$  in the  $(r, \Gamma)$  plane. The bifurcation diagrams at each of the three values of  $\Gamma$  labeled (i)–(iii) resemble those shown in Fig. 16. (b) As in (a), but for the type-II transition at  $\Gamma_{\phi=0}^{(9,10)}$ ; the labeled cuts resemble the bifurcation diagrams in Fig. 17. In each case the location of the reconnection event is indicated ( $\circ$ ). Saddle nodes associated with the snaking branch are plotted as solid lines, consistent with the convention in Figs. 16 and 17.

### III. ECKHAUS INSTABILITY

In this section we explain the relationship between the secondary bifurcations at either end of the snaking branches and the Eckhaus instability of spatially periodic states. We begin with a review of the Eckhaus results in the supercritical regime of Eq. (1), where  $|b_2|$  is sufficiently small that  $q_2 > 0$ . At small amplitude these states are described by Eq. (10) analyzed in Ref. [20]. The solution branch

$$A(X) = \sqrt{\frac{1}{q_2} \left( \frac{\mu}{4k_0^2} - Q^2 \right)} e^{iQX}, \quad (19)$$

which bifurcates supercritically from the trivial state at  $\mu = 4k_0^2 Q^2$ , corresponds in Eq. (1) to a branch of spatially periodic states with wave number  $k = k_0 + \epsilon Q$ . In a finite domain of size  $\Gamma$  only the spatially periodic branches with wave number  $k = 2\pi n / \Gamma$  are present so the allowed values of  $Q$  are discrete. In the previous section we labeled each branch using  $n$ , the number of wavelengths of the pattern that fit in the domain. In this section it is convenient to assign a new integer  $p \geq 0$  to each branch  $Q_p$  based on the ordering of the primary bifurcation points, so that  $\mu_p = 4k_0^2 Q_p^2$  is the  $(p+1)$ th bifurcation encountered as  $\mu$  increases. To determine the relation between the  $n$  and  $p$  labels of each branch, we note that a typical domain will not accommodate an integer number of wavelengths from the  $k_0$  branch and define the large integer  $N$  and the small number  $l$  by  $\Gamma = 2\pi(N-l)/k_0$ , where  $0 \leq |l| \leq 1/2$ . The special cases  $l=0, \pm 1/2$  involve degeneracies among the primary bifurcations  $\mu_p$  which complicate the enumeration but do not change the conclusions below. Furthermore, without loss of generality we can choose  $l > 0$  and therefore focus on the case  $0 < l < 1/2$ . The relations between the labels  $n$  and  $p$ , and the corresponding values of  $Q_p$ , are

$$n = \begin{cases} N + \frac{p}{2}, & p \text{ even,} \\ N - \frac{p+1}{2}, & p \text{ odd,} \end{cases}$$

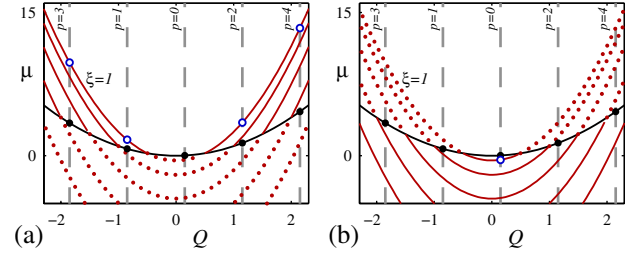


FIG. 19. (Color online) The Eckhaus instability for Eq. (10) when (a)  $q_2 > 0$  and (b)  $q_2 < 0$ . In (a) solutions with wave number  $k \neq k_0$  are stable above the Eckhaus boundary indicated by the symbol  $\circ$  for various values of the integer  $p \geq 1$ . The corresponding primary bifurcation points are denoted by  $\bullet$ . In (b) the primary bifurcations denoted by  $\bullet$  are subcritical, and solutions on the  $A_p$  branches are unstable. An Eckhaus ( $\xi=1$ ) instability is present on the  $p=0$  branch ( $\circ$ ).

$$Q_p = \begin{cases} k_0 \left( l + \frac{p}{2} \right), & p \text{ even,} \\ k_0 \left( l - \frac{p+1}{2} \right), & p \text{ odd.} \end{cases} \quad (20)$$

For example, the first primary bifurcation encountered is  $n = N$ , followed by  $n = N-1$ , then  $n = N+1$ . Between  $\mu_p$  and  $\mu_{p+1}$  the trivial state is unstable to  $p+1$  modes.

The branch  $A_p$  bifurcates supercritically at  $\mu_p$ . The stability properties of this branch are determined by writing  $A(X, T) = A_p(X) + \epsilon a_p(X) e^{\sigma T}$  and looking for neutrally stable solutions to the time-dependent version of Eq. (10) as  $\epsilon \rightarrow 0$ . In Ref. [20] it is shown that, near onset,  $A_p$  contains  $p$  unstable modes inherited from the trivial state. For  $p \geq 1$  these are enumerated by an integer  $\xi$  and can be written in the form

$$a_{p,\xi}(X) = [\alpha_{p,\xi} e^{ik_0 \xi X} + \beta_{p,\xi} e^{-ik_0 \xi X}] e^{iQ_p X}, \quad (21)$$

where  $0 < \xi \leq p$  and  $\alpha_{p,\xi}, \beta_{p,\xi}$  are real functions of  $\mu$ . The mode  $a_{p,\xi}$  has fundamental spatial period  $2\pi/\xi$  in  $X$ , or  $\Gamma/\xi$  in  $x$ . This mode stabilizes along  $A_p$  at  $\mu_{p,\xi}$ , where

$$\mu_{p,\xi} = 4k_0^2 \left( 3Q_p^2 - \frac{1}{2} \xi^2 \right). \quad (22)$$

The final mode to stabilize is  $\xi=1$ , and the  $A_p$  branch is stable in  $\mu > \mu_{p,1}$ . The bifurcation point  $\mu_{p,1}$  is referred to as the Eckhaus boundary for the  $A_p$  branch; in a domain with finite period  $\Gamma$  the Eckhaus instability present for  $\mu < \mu_{p,1}$  leads to spatial modulation of the pattern in the form of a single pulse as described by the mode  $a_{p,1}$ . In contrast, the secondary bifurcations at  $\mu_{p,\xi}$ ,  $\xi > 1$ , generate multipulse modulation. In fact, the Eckhaus instability is a subcritical pitchfork bifurcation that creates two new branches of stationary solutions in  $\mu > \mu_{p,1}$  and these extend to large  $r$  [20]. The locations of these bifurcation points are summarized in Fig. 19(a). The same analysis in the subcritical regime ( $q_2 < 0$ ) leads to the bifurcation structure shown in Fig. 19(b). In this case only the  $p=0$  branch contains an Eckhaus boundary. Other secondary bifurcations on the  $p=0$  branch, as well as

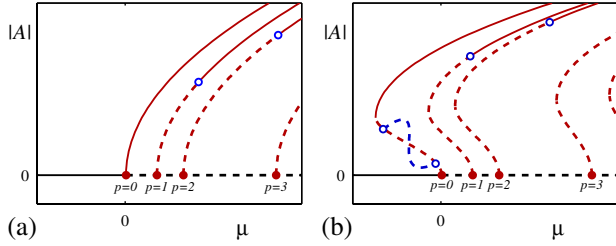


FIG. 20. (Color online) Sketch of the Eckhaus instability for Eq. (1) when (a)  $q_2 > 0$  and (b)  $q_2 < 0$ , including the saddle node bifurcations on each branch present when  $q_2 < 0$ . In (a) solutions with wave number  $k \neq k_0$  are stable above the Eckhaus boundary indicated by the symbol  $\circ$  for various values of the integer  $p \geq 1$ ; no Eckhaus instability is present on the  $p=0$  branch. The corresponding primary bifurcation points are denoted by  $\bullet$ . In (b) the primary bifurcations are subcritical and unstable; Eckhaus instabilities are present above the saddle nodes when  $p \geq 1$ , while for  $p=0$  a pair of Eckhaus points, connected by a snaking branch, is present.

all the secondary bifurcations on the  $p \neq 0$  branches, lead to multipulse modulation.

The connection to the results of the previous section is now clear. In the supercritical regime the Eckhaus instability is not present on the first spatially periodic branch ( $p=0$ ), but it is present in all other branches ( $p \geq 1$ ). When  $b_2$  is increased  $q_2$  becomes negative and the primary branches become subcritical, acquiring saddle nodes in the process (Fig. 20). As this happens the Eckhaus boundary remains at finite amplitude, typically above the new saddle nodes and the secondary branches continue to extend to large  $r$ . Thus for  $p \geq 1$  the Eckhaus boundary corresponds to the secondary bifurcations  $S^{(n')}$ .

The situation is different for the  $p=0$  branch. For this branch the change in criticality nucleates a pair of Eckhaus-type modes [Fig. 20(b)]. One of these remains near (typically below [21]) the saddle node and is identified with the point  $S^{(n')}$  on this branch; the other remains near the primary bifurcation and is identified with  $S^{(n)}$ . The secondary branches created in each of these two bifurcations are connected via a pair of snaking branches and do not extend to large  $r$ . With increasing  $b_2$  the behavior becomes more complicated as  $k_p$  and  $k_L$  start to differ from  $k_0$ , and transitions such as those in Fig. 2 become possible.

#### IV. EXAMPLE: NATURAL DOUBLY DIFFUSIVE CONVECTION

In this section we examine a more realistic, nonvariational, pattern-forming system and demonstrate that it behaves much like the simpler Swift-Hohenberg equation studied in the preceding sections. For this purpose we choose natural doubly diffusive convection in a vertical slot, the system in which spatially localized steady convection was in fact first identified [22,23]. This discovery used a two-dimensional formulation of the problem, reproduced below, and used direct numerical simulations of an enclosed container of aspect ratio  $\Gamma=7$  to find a numerically stable steady state consisting of a single cell located in the center of the

container. However, no attempt to understand the origin of this unexpected solution was made. It is now known [8,24] that states of this type are produced via homoclinic snaking, i.e., by the same process that is responsible for similar states in the Swift-Hohenberg equation. In the following we refer to these states as “convectons,” and focus on the simplest realization of this system, with periodic boundary conditions in the vertical [25]. We identify in this system the three critical wave numbers  $k_0$ ,  $k_p$ , and  $k_L$ , and show that the behavior of the snaking branches of localized states in this system is consistent with the description developed in Sec. II for the Swift-Hohenberg equation.

Natural doubly diffusive convection occurs as a result of applied horizontal gradients of temperature and concentration. We measure the relative importance of the temperature and concentration gradients by the buoyancy ratio  $N = \rho_C \Delta C / \rho_T \Delta T$ , where  $\rho_T < 0$ ,  $\rho_C > 0$  are the thermal and solutal “expansion” coefficients, and  $\Delta T$ ,  $\Delta C$  are the differences in temperature and concentration imposed across the system. When the imposed gradients are parallel, the two buoyancy forces are said to be cooperating if  $N > 0$  and opposing if  $N < 0$ .

The system is described by the dimensionless equations

$$\frac{\partial \mathbf{u}}{\partial t} = -(\mathbf{u} \cdot \nabla) \mathbf{u} - \nabla p + \text{Gr}(T + NC) \mathbf{e}_z + \nabla^2 \mathbf{u}, \quad (23)$$

$$0 = \nabla \cdot \mathbf{u}, \quad (24)$$

$$\frac{\partial T}{\partial t} = -(\mathbf{u} \cdot \nabla) T + \frac{1}{\text{Pr}} \nabla^2 T, \quad (25)$$

$$\frac{\partial C}{\partial t} = -(\mathbf{u} \cdot \nabla) C + \frac{1}{\text{Sc}} \nabla^2 C, \quad (26)$$

where  $\mathbf{u} = (u, w)$  and  $\nabla \equiv (\partial_x, \partial_z)$  in  $(x, z)$  coordinates, with  $x$  in the horizontal direction and  $z$  in the vertical direction. The Prandtl number  $\text{Pr}$ , the Schmidt number  $\text{Sc}$ , and the Grashof number  $\text{Gr}$  are defined by

$$\text{Pr} = \nu / \kappa, \quad \text{Sc} = \nu / D, \quad \text{Gr} = \frac{g \rho_T \Delta T l^3}{\nu^2}, \quad (27)$$

where  $\nu$  is the kinematic viscosity,  $\kappa$  is the thermal diffusivity,  $D$  is the solute diffusivity,  $g$  is the gravitational acceleration, and  $l$  is the slot width. The boundary conditions read

$$\text{at } x=0: \quad u = w = T - 1 = C - 1 = 0,$$

$$\text{at } x=1: \quad u = w = T = C = 0, \quad (28)$$

together with periodic boundary conditions with dimensionless period  $\Gamma$  in the  $z$  direction. Thus  $z$  plays the role of  $x$  in the Swift-Hohenberg equation of Sec. II. In the following we write  $T = 1 - x + \Theta$ ,  $C = 1 - x + \Sigma$  and examine the properties of the equations for  $u$ ,  $w$ ,  $\Theta$ , and  $\Sigma$ , focusing on the case  $N = -1$  for which these equations possess the trivial solution  $u = w = \Theta = \Sigma = 0$  for all values of  $\text{Gr}$ . The properties of this solution are the key to the nonlinear behavior of the system.

The equations for  $u$ ,  $w$ ,  $\Theta$ , and  $\Sigma$  are invariant under translations in  $z$  as well as a  $180^\circ$  rotation

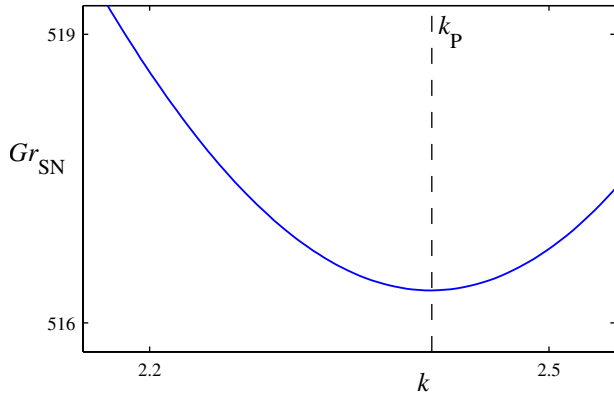


FIG. 21. (Color online) Locations of saddle node bifurcations  $Gr_{SN}$  measured on branches with several different wave numbers to determine  $k_p \approx 2.412$ .

$$\Delta:(x, z) \rightarrow (1 - x, -z), \quad (u, w, \Theta, \Sigma) \rightarrow -(u, w, \Theta, \Sigma), \tag{29}$$

where  $z=0$  is an arbitrarily chosen origin. It follows that the equations possess  $O(2)$  symmetry, the symmetry group of a circle under rotations (translations in  $z \bmod \Gamma$ ) and the ‘‘reflection’’  $\Delta$ . The presence of the symmetry  $\Delta$  implies that the problem is reversible in space, although here reversibility acts by  $-1$ , in contrast to the Swift-Hohenberg equation where it acts by  $+1$ . As a result all steady state bifurcations from the conduction state  $u=w=\Theta=\Sigma=0$  as  $Gr$  increases are pitchforks of revolution, and produce spatially periodic states with  $\Delta$  symmetry:

$$(u, w, \Theta, \Sigma)(1 - x, -z) = -(u, w, \Theta, \Sigma)(x, z). \tag{30}$$

Moreover, the leading spatial eigenvalues of the conduction state exhibit a reversible Hopf bifurcation with 1:1 resonance at  $Gr=Gr_0$  [24]: in  $Gr < Gr_0$  the eigenvalues form a complex quartet, at  $Gr=Gr_0$  they collide pairwise on the imaginary axis, and in  $Gr > Gr_0$  these eigenvalues split but remain purely imaginary. This bifurcation provided the key to the presence of localized states in the Swift-Hohenberg equation, and plays an equally important role for natural doubly diffusive convection. In particular, it follows that as  $Gr$  increases the trivial solution loses stability at  $Gr=Gr_0$  to spatially periodic states with wave number  $k_0$ . In the following we use the parameter values  $Pr=1$ ,  $Sc=11$  for which  $Gr_0 \approx 650.9$  and  $k_0 \approx 2.532$ , corresponding to wavelength  $\lambda_0 \approx 2.482$  [24]. For these parameters the bifurcation at  $Gr_0$  is subcritical and hence is accompanied by a pair of branches  $L_0, L_\pi$  of localized states just as in the Swift-Hohenberg equation.

In a finite but large periodic domain the first primary bifurcation occurs near  $Gr_0$  and produces a subcritical branch of periodic states with wavelength near  $\lambda_0$ . This bifurcation is followed in  $Gr > Gr_0$  by primary branches corresponding to other wave numbers  $k \neq k_0$ . Each branch in turn undergoes a saddle node bifurcation in  $Gr \ll Gr_0$ . The first saddle node encountered as  $Gr$  increases is located at  $Gr_{SN} \approx 516.3$  and occurs on the primary branch with wavelength  $\lambda_p \approx 2.605$ , or wave number  $k_p \approx 2.412$  (Fig. 21).

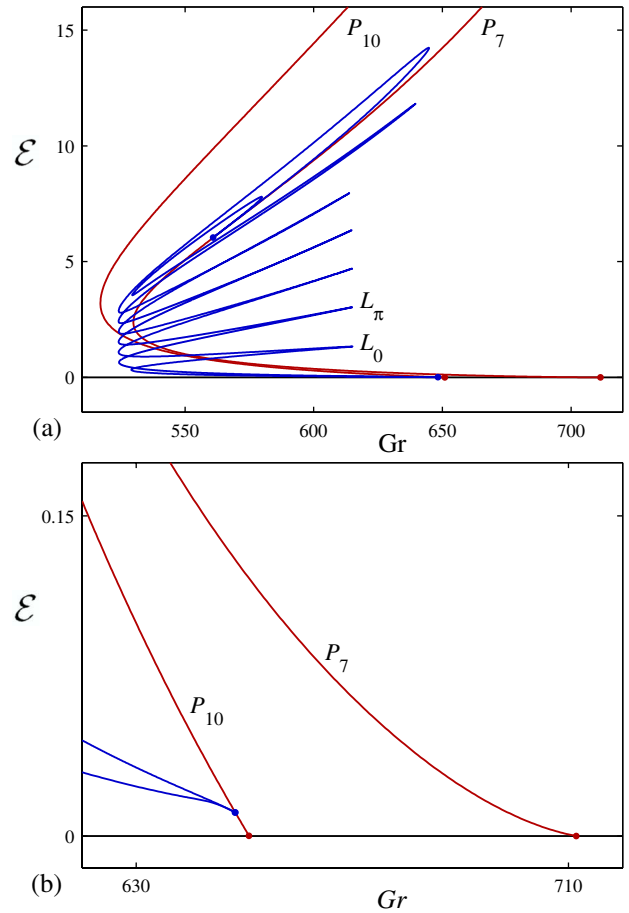


FIG. 22. (Color online) Bifurcation diagram for  $\Gamma=10\lambda_0$ : both snaking branches terminate on  $P_7$  at the location indicated by  $\bullet$ .

To explore the behavior of localized states in such a system we first compute the allowed primary spatially periodic branches permitted by the finite domain period  $\Gamma$ . We also track the stability changes along these branches and use them to identify secondary bifurcations of the type that lead to localized states. These are then used to initialize the branch-following code to compute branches of localized states. Stationary solutions are plotted in bifurcation diagrams in terms of their dimensionless kinetic energy  $\mathcal{E} \equiv \frac{1}{2} \int_0^\Gamma \int_0^1 (u^2 + w^2) dx dz$ .

Figure 22 shows the bifurcation diagram corresponding to a  $\Gamma=24.82$  periodic domain. The branches are labeled using the notation  $P_n$  to indicate periodic states with  $n$  wavelengths in the domain period  $\Gamma$ . Since  $\Gamma=24.82$  admits exactly ten wavelengths  $\lambda_0$ , the first primary branch is therefore the branch  $P_{10}$ . Near onset these states consist of both clockwise and counterclockwise rolls, but with increasing amplitude the counterclockwise rolls weaken and disappear leaving only clockwise rolls [8]. The  $P_{10}$  branch undergoes a secondary bifurcation at small amplitude which produces a pair of localized branches  $L_0$  and  $L_\pi$ . Near onset the profiles along these branches resemble the  $P_{10}$  convective state, but the strength of the rolls is modulated across the domain. On the  $L_0$  branch this modulation strengthens the clockwise roll in the center of the domain; with increasing modulation amplitude (decreasing  $Gr$ ) this state evolves into a single clock-

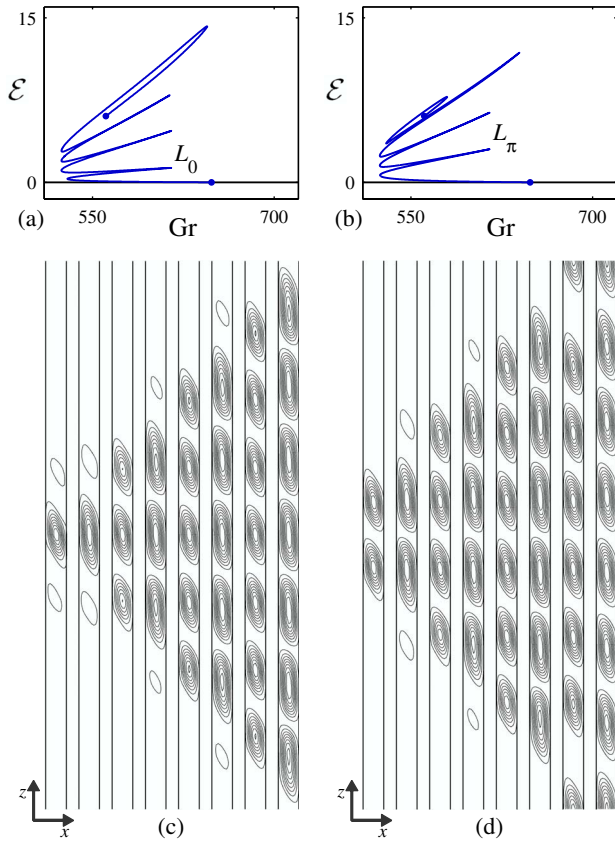


FIG. 23. (Color online) The two snaking branches  $L_0$  (a), (c) and  $L_\pi$  (b), (d) together with the corresponding solution profiles when  $\Gamma = 10\lambda_0$ . The profiles are shown at successive saddle nodes starting from lowest energy  $\mathcal{E}$  (left to right).

wise convective roll embedded in an otherwise conducting background state. Far from onset the  $L_0$  branch undergoes snaking as the profile grows in extent by the pairwise addition of rolls, one roll on each side. Thus the  $L_0$  branch consists of solutions with an odd number of rolls and the midpoint of the localized state is located at the center of a clockwise roll [Fig. 23(c)]. On the  $L_\pi$  branch the modulation initially strengthens a counterclockwise roll, but once such rolls are suppressed at larger amplitude the result is the strengthening of a pair of adjacent clockwise convective rolls in the center of the domain. The  $L_\pi$  branch also begins to snake far from onset once the solution starts adding rolls pairwise. The resulting solution profiles always contain an even number of rolls, and the midpoint of each state lies between the two central clockwise rolls [Fig. 23(d)]. By identifying clockwise rolls with local peaks of the amplitude  $u(x)$  in the Swift-Hohenberg equation, we can identify  $L_0$  ( $L_\pi$ ) with the branches of the same name from Sec. II.

At other values of  $\Gamma$  we observe similar small amplitude behavior: the only spatially periodic branch that undergoes a secondary bifurcation to states with fundamental spatial period  $\Gamma$  is the first branch encountered as  $Gr$  increases, i.e., the branch with wave number closest to  $k_0$ , and this secondary bifurcation leads to a pair of snaking branches  $L_0$ ,  $L_\pi$ . Thus the small amplitude behavior is completely analogous to the behavior of the Swift-Hohenberg equation.

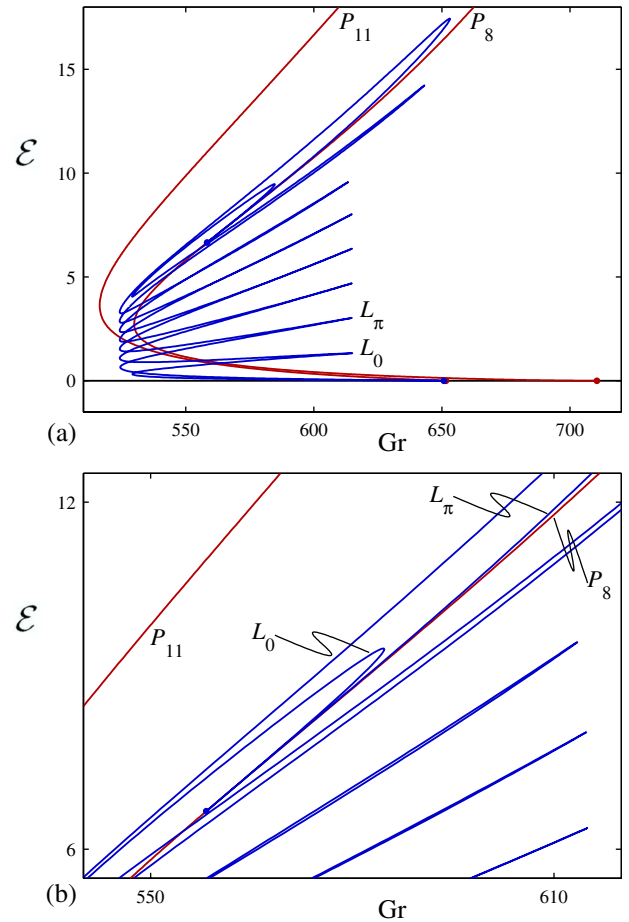


FIG. 24. (Color online) Bifurcation diagram for  $\Gamma = 11.4\lambda_0$ : both snaking branches terminate on  $P_8$  at the location indicated by  $\bullet$ .

We next report on the secondary bifurcations at large amplitude and the termination of the two snaking branches. The crucial wave number  $k_L$  for this process is found by examining wave number selection within the pinning region, located between  $Gr \approx 524.2$  and  $Gr \approx 614.9$ . The selected wavelength varies between  $\lambda_- \approx 3.07$  at the left edge of the pinning region and  $\lambda_+ \approx 3.37$  (or  $\lambda_+ \approx 1.36\lambda_0$ ) at the right, corresponding to  $k_L \approx 1.87$  or  $k_L \approx 0.737k_0$ . We expect the two snaking branches to terminate together on the spatially periodic branch with wave number closest to  $k_L$  provided such a branch is present. The domain period in Fig. 22 is large enough to fit seven of these wavelengths  $\Gamma \sim 7 \times 2\pi/k_L$  and both  $L_0$  and  $L_\pi$  do in fact terminate on the  $P_7$  branch.

Figure 24 shows the bifurcation diagram in a  $\Gamma = 11.4\lambda_0$  periodic domain, which is large enough for the snaking branches to fit one extra roll at termination ( $\Gamma \sim 8 \times 2\pi/k_L$ ). As expected the bifurcation diagram is quite similar to that in Fig. 22: the two snaking branches bifurcate together from  $P_{11}$  at small amplitude, and terminate together on the spatially periodic branch with wave number closest to  $k_L$ , in this case the  $P_8$  branch. In Fig. 25 we show the details of the branch  $P_9$  which bifurcates from the trivial solution between  $P_{11}$  and  $P_8$ . The figure shows that at large amplitude the  $P_9$  undergoes a (pitchfork) bifurcation to a pair of mixed mode branches. These branches increase monotonically with increasing  $Gr$ . As in the other secondary bifurcations we have

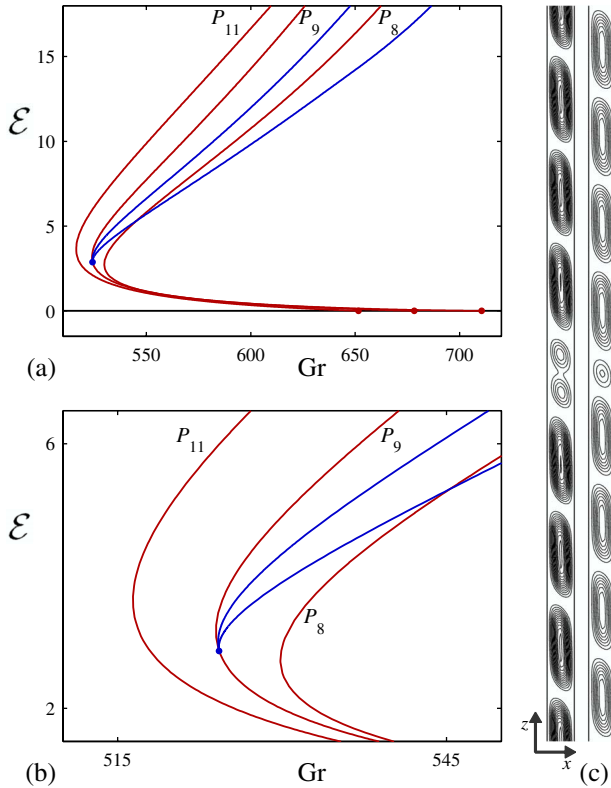


FIG. 25. (Color online) Bifurcation diagram for  $\Gamma=11.4\lambda_0$ : the two unlabeled branches are the mixed mode branches that emerge from  $P_9$  at the location indicated by  $\bullet$ . The side panels on the right show sample solutions on these branches at  $Gr \approx 700$ .

discussed the corresponding solutions are not related by symmetry. We show two typical solutions at large  $Gr$  in Fig. 25(c).

Consider next the transition that occurs as  $\Gamma$  increases from  $\Gamma \sim 7 \times 2\pi/k_L$  (Fig. 22) to  $\Gamma \sim 8 \times 2\pi/k_L$  (Fig. 24). In the former case both  $L_0$  and  $L_\pi$  terminate on the  $P_7$  branch while in the latter they terminate on the  $P_8$  branch. In the following we start with Fig. 24 and increase  $\Gamma$ . Figure 26 shows the bifurcation for  $\Gamma=11.6\lambda_0$ . At this value of  $\Gamma$  the localized states bifurcate from a secondary bifurcation on the  $P_{12}$  branch, but the  $L_\pi$  branch still terminates on  $P_8$ . On the other hand the  $L_0$  branch now terminates on  $P_9$ . Thus while the localized branches appear together at small amplitude they now terminate on different branches of periodic states. This observation is in qualitative agreement with the more complete results for the Swift-Hohenberg equation presented in Sec. II B. However, there are also some differences. Figure 26 shows that prior to termination on  $P_8$  the  $L_\pi$  branch executes a large excursion, larger than the excursion visible already in Fig. 24. To understand the origin of this behavior (which is absent from the Swift-Hohenberg equation) we have computed the bifurcation diagram for  $\Gamma=10.5\lambda_0$ . Because of the approximate periodicity in  $\Gamma$  seen already in Figs. 4 and 13 this value of  $\Gamma$  is expected to correspond to increasing  $\Gamma$  above  $11.6\lambda_0$  with appropriate relabeling of the branches and an exchange in the roles played by  $L_0$  and  $L_\pi$ . Indeed, we find that at  $\Gamma=10.5\lambda_0$  the  $L_\pi$  branch terminates on  $P_8$  (analogous to the termination of the  $L_0$  branch on  $P_9$  at

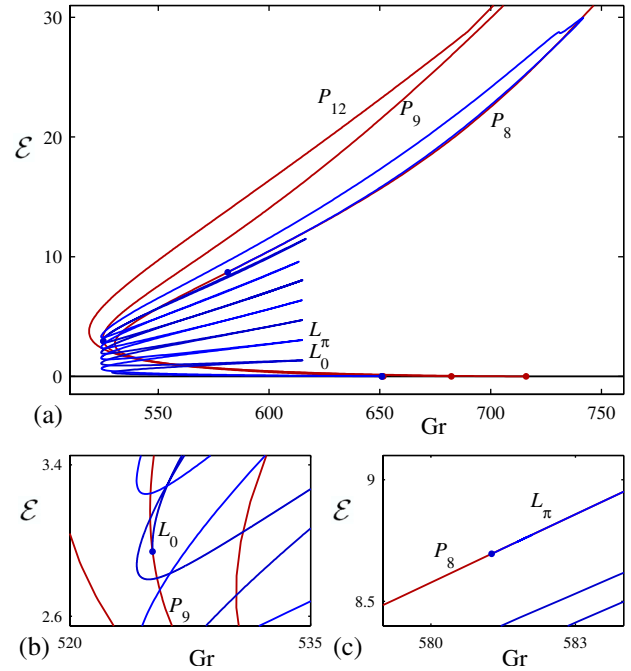


FIG. 26. (Color online) Bifurcation diagram for  $\Gamma=11.6\lambda_0$ : the  $L_0$  branch terminates on  $P_9$  while  $L_\pi$  terminates on  $P_8$ . Both termination points are indicated by  $\bullet$ .

$\Gamma=11.6\lambda_0$ ) while the  $L_0$  branch extends to large  $Gr$  (analogous to the large excursion of  $L_\pi$  for  $\Gamma=11.6\lambda_0$ ). This time, however, the  $L_0$  branch continues monotonically to large  $Gr$  and does not return to terminate on  $P_7$ . Evidently the  $L_0$  branch now connects to a mixed mode branch, and this branch is the secondary branch that bifurcates from  $P_8$  for values of  $\Gamma$  closer to  $\Gamma=10\lambda_0$ . The identification of the large  $Gr$   $L_0$  branch as the mixed mode branch originating from  $S^{(8)}$  on  $P_8$  is confirmed in Fig. 27(d) which shows a solution profile at  $Gr \approx 900$  for comparison with the corresponding solution profiles on the mixed mode branches bifurcating from  $S^{(9)}$  on  $P_9$  shown in Fig. 25. We understand this behavior, which does not occur in the Swift-Hohenberg equation, in terms of a new two-step transition shown schematically in Fig. 28. In this transition the interaction of the two secondary branches results first in a connection between the localized ( $L$ ) and mixed mode ( $M$ ) subbranches, and a connection between the  $n'$  and  $n'+1$  subbranches, implying that the  $L$  branch now extends to large  $Gr$  becoming a mixed mode state  $M$  instead of terminating. A subsequent interaction between the same two branches forms a connection between the  $L$  and  $n'+1$  subbranches, and the  $M$  and  $n'$  subbranches, allowing the snaking branch to terminate again on a spatially periodic branch. The net effect of the two-step process shown in Fig. 28 and the one-step process shown in Fig. 16 is the same, but the two-step transition allows for the observed range of  $Gr$  values in which the snaking branch does not terminate. Although we do not understand in detail the reason for the difference in the transitions observed in the Swift-Hohenberg equation and in the doubly diffusive convection problem, it is apparent that in the latter it is “energetically” favorable to allow the wave number of the pattern to adjust as  $Gr$  increases even at the expense of retaining a

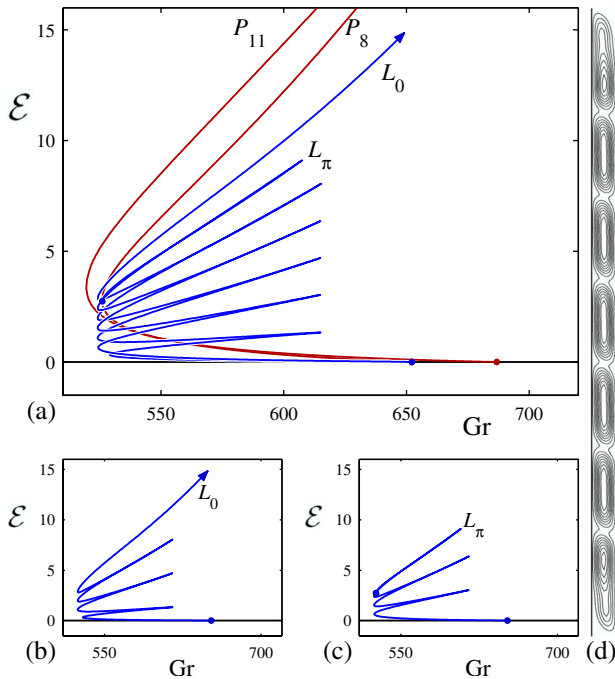


FIG. 27. (Color online) Bifurcation diagram for  $\Gamma = 10.5\lambda_0$ ; the  $L_0$  branch continues to large  $Gr$  as a mixed mode branch while  $L_\pi$  terminates on  $P_8$  at the location indicated by  $\bullet$ . The right panel shows a mixed mode solution at  $Gr \approx 900$ .

defect [Fig. 27(d)]. In contrast, the variational nature of the Swift-Hohenberg equation favors a uniform wave number in the pattern and hence no defect, albeit at the expense of a nonoptimal wave number.

We have also examined the behavior of the termination point of the snaking branches at several other values of  $\Gamma$ . Although incomplete, the results confirm the two-step branch switching process summarized in Fig. 28 and suggest that the transition between the termination of the  $L_0$  branch when  $\Gamma = 11.4\lambda_0$  (Fig. 24) and on  $P_9$  when  $\Gamma = 11.6\lambda_0$  (Fig. 26) occurs via a one-step process of the type observed in the Swift-Hohenberg equation, i.e., the type-I transition in the doubly diffusive problem is a one-step transition resembling that in the Swift-Hohenberg equation, while the type-II transition becomes a two-step process.

**V. DISCUSSION AND CONCLUSIONS**

Homoclinic snaking in bistable systems that are unbounded in one spatial dimension is now well understood

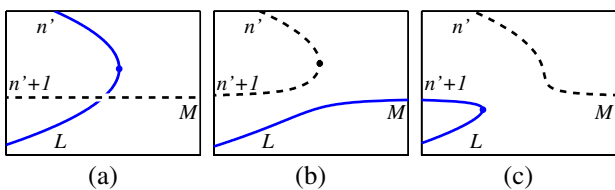


FIG. 28. (Color online) Sketch showing a two-step transition. By comparison, the one-step process in Fig. 16 transitions from (a) to (c) directly, without ever forming a connection between the  $L$  and  $M$  subbranches. Hysteresis bifurcations are omitted. Notation is the same as Fig. 16.

[26]. In particular, in systems without additional symmetries two branches of spatially localized states bifurcate from the trivial state together with the primary branch of spatially periodic states, a consequence of the presence of the 1:1 reversible Hopf bifurcation of the trivial state in space. All three of these branches bifurcate subcritically and are initially unstable. However, in experiments or in numerical simulations the available domain is never infinite, and the constraints imposed by a finite domain affect both the birth and disappearance of spatially localized states. In this paper we have examined the effects of an imposed large but finite spatial period, using both a model pattern-forming system and a numerical example from fluid dynamics, namely natural doubly diffusive convection in a vertical slot. We have seen that the presence of a finite spatial period  $\Gamma$  modifies the small amplitude localized states present when  $|r| < O(k_0^2 \Gamma^{-2})$ . In particular, the branches of localized states no longer bifurcate from the trivial or conduction state. Instead they typically form as a result of a secondary bifurcation of the *first* spatially periodic pattern that sets in, as observed already in Refs. [27,28]. This instability is generically a pitchfork bifurcation, and produces a pair of branches of spatially modulated periodic states with spatial period  $\Gamma$ . Despite their origin in a pitchfork bifurcation these states are not related by symmetry. The states produced in this bifurcation are initially only weakly localized, but evolve into strongly localized states by the time the branch enters the snaking or pinning region.

The effect of the finite period is more striking at the other end of the snaking branches, where the localized states almost fill the available spatial period, forcing the snaking to terminate. We have seen that in this regime the branches of localized states turn over, exit the snaking region and terminate on a branch of spatially periodic states whose wave number depends critically on the domain size but is typically close to  $k_L$ , the smallest wave number associated with the localized structures in the pinning region. This termination point is also a pitchfork bifurcation and can be on the same branch from which the localized states bifurcated initially or on another periodic branch; the latter is inevitable in large domains due to the difference between  $k_0$  and  $k_L$ . The termination point can lie below or above the saddle node on the spatially periodic branch, but in large domains will generally lie above the saddle node owing to the difference between  $k_p$  and  $k_L$ . Here  $k_p$  is the wave number minimizing the parameter value corresponding to the saddle node of the periodic states. Moreover, we have seen that the two snaking branches are always created together at small amplitude from the same spatially periodic branch but that at large amplitude the two can “unzip” and terminate on different branches (Fig. 2). Since the termination points are pitchforks the single terminations are necessarily accompanied by a second branch which does not snake. We have shown that these branches correspond to mixed modes and extend to large  $r$ . In fact as we saw in the doubly diffusive problem the snaking branches need not terminate at all, and instead may follow a branch of periodic states to large amplitude. Heuristically this occurs whenever an integer number of wavelengths near  $2\pi/k_L$  leaves space that is too small for the insertion of an additional roll, and the systems finds that it is “energetically”

favorable to retain the basic wavelength of the existing rolls at the expense of including a defect in the periodic pattern. In this case the solutions on the snaking branch evolve continuously with increasing amplitude into the defectlike mixed mode states.

Analogous secondary bifurcations on other branches of periodic solutions lead to pairs of mixed mode branches that also extend to large  $r$ . In all cases these states are subcritical in the sense that they bifurcate in the direction of increasing stability. The bifurcations responsible for the mixed modes, as well as those responsible for the beginning and end of each snaking branch, all correspond to Eckhaus-type (i.e., a long wave) instability of the relevant periodic state. Moreover, these Eckhaus-like instabilities are nucleated pairwise on the primary subcritical branch as the subcriticality of the periodic branch increases. In particular, if the extent of bistability is small, both snaking branches appear and end together.

The present work remains incomplete in two important aspects. We have not specified in detail the stability properties of the various branches we compute. In the Swift-Hohenberg equation the stability assignments are simple to

deduce since one knows that the same eigenvalue is always responsible for the stability changes that take place at the saddle nodes, and this property remains true in the large periodic domains we consider, as verified by explicit stability computations [11]. In the doubly diffusive problem we keep track of the dominant eigenvalues of each state using Arnoldi's method. Here eigenvalues can be complex and oscillatory (Hopf) bifurcations may be present. We have in addition limited the work to so-called single pulse localized states, consisting of a single localized structure in a spatial period. Of course, multipulse states consisting of equally and unequally spaced localized structures exist also, adding immeasurably to the complexity of the solution space. These will be described elsewhere.

#### ACKNOWLEDGMENTS

This work was supported by the National Science Foundation under Grant No. DMS-0605238 and a CNRS Projet International de Cooperation Scientifique (Grant No. PICS-3471).

- 
- [1] P. B. Umbanhowar, F. Melo, and H. L. Swinney, *Nature (London)* **382**, 793 (1996).
  - [2] O. Lioubashevski, Y. Hamiel, A. Agnon, Z. Reches, and J. Fineberg, *Phys. Rev. Lett.* **83**, 3190 (1999).
  - [3] K. J. Lee, W. D. McCormick, J. E. Pearson, and H. L. Swinney, *Nature (London)* **369**, 215 (1994).
  - [4] A. G. Vladimirov, J. M. McSloy, D. V. Skryabin, and W. J. Firth, *Phys. Rev. E* **65**, 046606 (2002).
  - [5] R. Richter and I. V. Barashenkov, *Phys. Rev. Lett.* **94**, 184503 (2005).
  - [6] O. Batiste and E. Knobloch, *Phys. Rev. Lett.* **95**, 244501 (2005).
  - [7] O. Batiste, E. Knobloch, A. Alonso, and I. Mercader, *J. Fluid Mech.* **560**, 149 (2006).
  - [8] A. Bergeon and E. Knobloch, *Phys. Fluids* **20**, 034102 (2008).
  - [9] S. Blanchflower, *Phys. Lett. A* **261**, 74 (1999).
  - [10] S. Blanchflower and N. Weiss, *Phys. Lett. A* **294**, 297 (2002).
  - [11] J. Burke and E. Knobloch, *Phys. Rev. E* **73**, 056211 (2006).
  - [12] J. Burke and E. Knobloch, *Phys. Lett. A* **360**, 681 (2007).
  - [13] M. Beck, J. Knobloch, D. J. B. Lloyd, B. Sandstede, and T. Wagenknecht (unpublished).
  - [14] G. W. Hunt, M. A. Peletier, A. R. Champneys, P. D. Woods, M. Ahmer Wadee, C. J. Budd, and G. J. Lord, *Nonlinear Dyn.* **21**, 3 (2000).
  - [15] G. Kozyreff and S. J. Chapman, *Phys. Rev. Lett.* **97**, 044502 (2006).
  - [16] P. Couillet, C. Riera, and C. Tresser, *Chaos* **14**, 193 (2004).
  - [17] M. C. Cross, P. G. Daniels, P. C. Hohenberg, and E. D. Siggia, *J. Fluid Mech.* **127**, 155 (1983).
  - [18] M. Golubitsky and D. G. Schaeffer, *Singularities and Groups in Bifurcation Theory* (Springer, New York, 1984), Vol. 1.
  - [19] J. Prat, I. Mercader, and E. Knobloch, *Int. J. Bifurcation Chaos Appl. Sci. Eng.* **12**, 281 (2002).
  - [20] L. S. Tuckerman and D. Barkley, *Physica D* **46**, 57 (1990).
  - [21] P. Couillet, E. Risler, and N. Vandenberghe, *J. Stat. Phys.* **101**, 521 (2000).
  - [22] K. Ghorayeb, Thèse de Doctorat de l'Université Paul Sabatier, Toulouse 3, France, 1997.
  - [23] K. Ghorayeb and A. Mojtabi, *Phys. Fluids* **9**, 2339 (1997).
  - [24] A. Bergeon and E. Knobloch, *Physica D* **237**, 1139 (2008).
  - [25] S. Xin, P. Le Quééré, and L. S. Tuckerman, *Phys. Fluids* **10**, 850 (1998).
  - [26] J. Burke and E. Knobloch, *Chaos* **17**, 037102 (2007).
  - [27] W. J. Firth, L. Columbo, and T. Maggipinto, *Chaos* **17**, 037115 (2007).
  - [28] Y. Hiraoka and T. Ogawa, *Jpn. J. Ind. Appl. Math.* **22**, 57 (2005).